Numerical and experiment study on ventilation performance of the equipment compartment of Alpine high-speed train

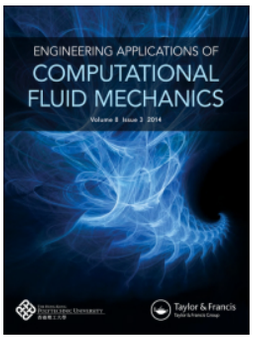

Taylor & Francis
Taylor & Francis Group

Engineering Applications of Computational Fluid Mechanics

ISSN: (Print) (Online) Journal homepage: https://www.tandfonline.com/loi/tcfm20

Numerical and experiment study on ventilation performance of the equipment compartment of Alpine high-speed train

Yitong Wu, Wei Zhou, Xifeng Liang, Dawei Chen, Xinchao Su, Xiaobai Li, Fan Wu & Sinisa Krajnović

To cite this article: Yitong Wu, Wei Zhou, Xifeng Liang, Dawei Chen, Xinchao Su, Xiaobai Li, Fan Wu & Sinisa Krajnović (2023) Numerical and experiment study on ventilation performance of the equipment compartment of Alpine high-speed train, Engineering Applications of Computational Fluid Mechanics, 17:1, 2252514, DOI: 10.1080/19942060.2023.2252514

To link to this article: https://doi.org/10.1080/19942060.2023.2252514

Published online: 31 Aug 2023.

ENGINEERING APPLICATIONS OF COMPUTATIONAL FLUID MECHANICS
2023, VOL. 17, NO. 1, 2252514
https://doi.org/10.1080/19942060.2023.2252514

Numerical and experiment study on ventilation performance of the equipment compartment of Alpine high-speed train

Yitong Wu[a,b,c], Wei Zhou[a,b,c], Xifeng Liang[a,b,c], Dawei Chen[d], Xinchao Su[a,b,c], Xiaobai Li[a,b,c], Fan Wu[a,b,c] and Sinisa Krajnović[e]

[a]Key Laboratory of Traffic Safety on Track, Ministry of Education, School of Traffic & Transportation Engineering, Central South University, Changsha, People's Republic of China; [b]Joint International Research Laboratory of Key Technology for Rail Traffic Safety, Central South University, Changsha, People's Republic of China; [c]National & Local Joint Engineering Research Center of Safety Technology for Rail Vehicle, Changsha, People's Republic of China; [d]China Railway Rolling Stock Corporation Qingdao Sifang Co., Ltd., Qingdao, People's Republic of China; [e]Division of Fluid Dynamics, Department of Mechanics and Maritime Sciences, Chalmers University of Technology, Gothenburg, Sweden

ABSTRACT

Alpine High-Speed Train serves on the Lanzhou-Urumqi Line in northwest China, where the terrain is mainly the Gobi Desert. To adapt to this complex environment, the independent-air duct is mainly used for the electrical facilities inside the equipment compartment to prevent the spread of sand particles. This isolated air duct makes ventilation characteristics of the equipment susceptible to the external environment. For this reason, this work aims to clarify and investigate the ventilation characteristic of electrical facilities. A two-step simulation method using IDDES (Improved Delayed Detached Eddy Simulation) and a real-vehicle tracking test using the T-typed pitot tubes were conducted. In the simulation, it is found that the ventilation performance can be influenced by the location of the equipment compartment, facilities and the fan mounted inside. By comparing the results of the test and simulation, they share the same characteristic that the air outlet volume of the converter near the head car is being promoted while it near the tail car is being inhibited. The maximum deviation ratio between the test and simulation is 9%. Therefore, the measurement method in this study is relatively reliable.

ARTICLE HISTORY
Received 21 June 2023
Accepted 19 August 2023

KEYWORDS
Alpine High-Speed Train; equipment compartment; independent air duct; ventilation performance

1. Introduction

High-speed trains (HSTs) are electrically powered and produce no greenhouse gases or air pollutants, which rely on a comprehensive power system containing many electrical facilities, such as converters, transformers, traction motors, etc. They are housed in an enclosed cabin called the equipment compartment (EC), which is located underneath the train (Zhou et al., 2019). The ventilation air vents of EC contain grilles and filters, to protect the internal electrical facilities from foreign particles (Feng et al., 2022). This relatively closed environment of the EC makes it difficult to exhaust the thermal airflow generated by the operation of electrical facilities, and the heat accumulates. Once the temperature of the equipment exceeds the safe limits, it will affect the operation of facilities, for example, causing a secondary breakdown of facilities and then incurring a short circuit failure (Yang et al., 2010), and causing irreversible demagnetisation of the permanent magnets (Shen et al., 2018). Favourable ventilation of electrical equipment can prevent them from failing and short circuits (Zhang et al., 2017), assuring their working performance and operation safety (Barone et al., 2020; Jia et al., 2016).

The air-forced cooling technology is mainly used to chill the electrical facilities in the EC of Alpine HST. Ambient air is drawn into the air ducts of the electrical facilities by fans, which enhances ventilation performance (Asadi & Arezi, 2011). Alpine HST serves on the Lanzhou-Urumqi Line in northwest China, where the terrain is mainly the Gobi Desert and the maximum wind speed can reach 20 m/s (Yao et al., 2012). To adapt to this complex environment, the EC of Alpine HST has been retrofitted with a sand-proof design. One of the sand-proof designs for the electrical facilities is the independent-air duct, as shown in Figure 1. The independent-air duct contains a deflector shield between the air vents of the EC and the inlet and outlet of the converter. It means the air duct is isolated from the EC and directly connected to the external environment, which prevents the flow-in sand spread in the EC. Nevertheless,

CONTACT Wei Zhou zhou_wei000@126.com; Xinchao Su suxinchao@csu.edu.cn Key Laboratory of Traffic Safety on Track, Ministry of Education, School of Traffic & Transportation Engineering; Central South University, Changsha 410075, China

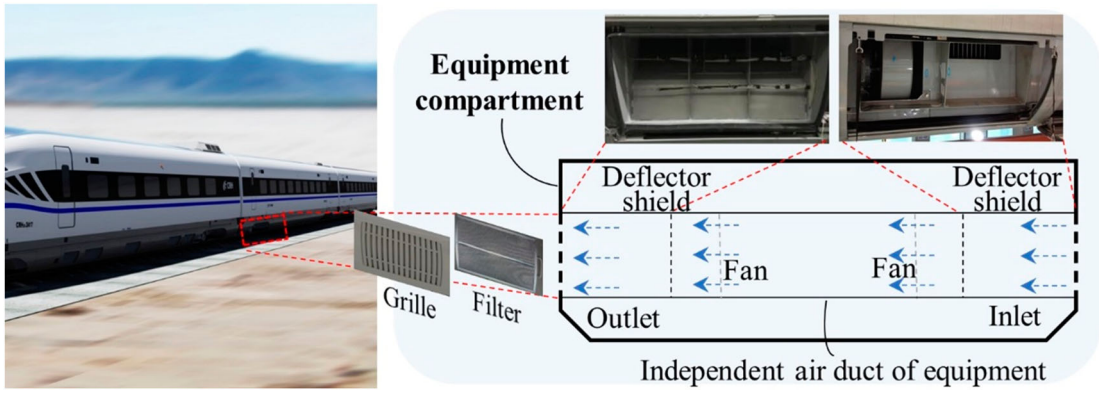

Figure 1. The structure diagram of the independent air duct inside the converter.

this isolated air duct makes the ventilation characteristics of the equipment susceptible to the external environment. In this case, the airflow inside the EC cannot be supplied to the facilities' air duct as an additional air source when some of the facilities have insufficient air intake due to their unfavourable installation location and the complex external flow fields (Ferranti et al., 2016; Pan et al., 2021). In addition, when trains are operating for a long duration, the filters at the air vents become clogged with sand particles (Kotelnikov et al., 2017). As the running time increases, the blockage aggravates, making it difficult for airflow to enter the ducts and hampering the ventilation effect of the equipment (Tanghong & Gang, 2010). Therefore, it is necessary to adjust the existing filter replacement intervals.

Some experiments and field tests of ventilation measurement have been conducted in previous studies. A series of ventilation measurements were carried out using omnidirectional velocity probes that were installed around the heated manikin inside the passenger cabin of the train in different ventilation systems (Maier et al., 2017; Schmeling & Bosbach, 2017). The accuracy of the omnidirectional velocity probes is better within the measurement range from 0.05 m/s to 1 m/s. A velocity measurement is performed by 5-hole pressure probes and hot-wires anemometry (Paradot et al., 2009). The measurement results have significant errors at the roof and underbody levels due to the complicated flow field (Kaltenbach et al., 2008). For an airflow measurement tool, the S-type pitot tube, the coefficient deviation is less than 0.3% in the range of $3000 < Re < 22{,}000$ (Kang et al., 2015). The measurement devices mentioned above provide great accuracy in low airflow velocity measurement. As the airflow of the EC underneath the train is complicated (Suzuki et al., 2008; Wang et al., 2021), especially when the train is running at a high speed, the above devices are not appropriate. Benjamin proposed correction factors of the hot wire anemometer, to make it available in the velocity range of 0–14 m/s and temperature range of 300–500 K (Benjamin & Roberts, 2002). The measuring probe material of the hot-wire anemometer is a very thin metal wire, which is easily damaged by sand particles (Comte-Bellot, 1976). Additionally, the irregular shape of the air vent (López González et al., 2014), and the blocking effect of measuring devices when installed in the limited area of the air vent (Wang et al., 2022) will affect the measurement accuracy. Georgiou presented a sub-miniature multi-hole pressure probe which enables its placement within confined and complex geometry areas (Georgiou & Milidonis, 2014). This probe needs to be equipped with 5 differential pressure sensors, which adds measurement costs considerably when there are many measurement points.

On the contrary, numerical calculation shows great advantages in the ventilation studies of the EC, to easily capture the internal flow characteristics of the EC, and without the limitations of test devices measurement conditions. In this regard, some research on the ventilation performance of the cabin and equipment has been studied numerically. The temperature field simulation of the EC shows that the maximum average surface temperature of heat-generated equipment is up to 56.5âĎČ (Jia et al., 2015). In addition, the outdoor environment condition has a significant effect on the indoor environment of the train cabin (Li, 2020; Li & Wang, 2015; Liu et al., 2011). The condensing air flux of air-conditioning units on the top of the HST was greatly affected during the train operation at the higher speed (Li et al., 2019). Moreover, the volume flow rate of fresh air is a key factor in indoor air quality in the train passenger cabin (Bai & Gong, 2012). The wind speed, temperature and gas concentration of the passenger cabin indoor environment were simulated, to design the air supply schemes of the air-conditioning system (Yang et al., 2017). And the air distribution systems in three different train passenger cabins in China were investigated (Wang et al.,

2014). From the above studies, the ventilation of the internal environment would be influenced by the external environment conditions. The study of the flow field characteristics in the internal environment can be used as a design guideline for the ventilation system supply air scheme. Most studies in the field of internal environment ventilation performance of HST were mainly focused on the passenger cabin. Although some studies concentrate on the ventilation performance of the EC, they usually ignore the effects of the ventilation equipment of the electrical facilities on the overall ventilation performance of the EC. The studies on the external environment underneath the train were mainly concentrated on the flow characteristics around the train's bogies (Soper et al., 2018; Zhang et al., 2016; Zhu & Hu, 2017). Bogies will increase the velocity magnitude, velocity gradient and turbulent intensity of the underbody flow (Wang et al., 2019; Wang, Burton, et al., 2018). The train with enclosed bogie cavities/inter-carriage gaps could decrease the aerodynamic drag (Wang, Zhang, et al., 2018; Zhang, Adamu, et al., 2022). To improve the ventilation of the electrical facilities and EC, the external and internal flow field characteristics of it need to be further investigated.

The difficulties of research on ventilation characteristics through literature research are summarised as follows:

(1) For the airflow measurement in the EC, the measurement devices should have high accuracy in complex flow fields and high-temperature environments. It should not be easily damaged by sand impacts. Moreover, it can meet the installation requirements of arranging multiple measurement points in a limited space.
(2) There are many factors that influence the ventilation effect. It is greatly influenced by the flow state of the external environment, especially in the high-speed flow field. While the study on the ventilation characteristic and the airflow measurement of the electrical facilities and EC in different locations are limited.
(3) The effects of the ventilation equipment inside the electrical facilities on the overall ventilation performance of the EC are ignored. The electrical facilities containing ventilation equipment and air duct structures are needed to further modelling. Moreover, it will increase the number of meshes and computational resources, to simulate the flow field containing a long formation train and electrical facilities, with the assurance that detailed flow features can be captured.

For this reason, this work aims to clarify and investigate the ventilation characteristic of electrical facilities and EC using numerical calculation and real-vehicle tests. Concretely:

(1) A two-step simulation method using the IDDES model is carried out, to capture details of the flow characteristics around the EC more economically.
(2) The effects of the ventilation equipment inside the electrical facilities on the overall ventilation performance of the EC are considered.
(3) The ventilation performance of ECs in different locations is characterised, to provide recommendations for the ventilation equipment arrangement and design.
(4) T-type pitot tubes (TTPT) are adopted in the airflow measurement of a real-vehicle test. The TTPT is a bendable and miniature pitot tube that facilitates the installation of multiple measuring points at a limited area of ventilation air vents.
(5) The effect of clogged filters on ventilation is monitored during the test, to provide a recommendation for filter replacement intervals.

2. Methodology

2.1. Geometry models

2.1.1. Alpine HST model

The model of the train is based on the operating Alpine HST, composed of a head car, a tail car and six middle cars. The length (L), height (H) and width (W) of the train are 201.39, 3.86 and 3.33 m, respectively. As shown in Figure 2, the details of bogies are retained, and the pantographs of the train and rail models are not included in this simulation.

2.1.2. EC model

The head and the tail cars are trailers without electrical facilities in the ECs. Therefore, the ECs in the 2nd car and 7th car are chosen for the research objects in this

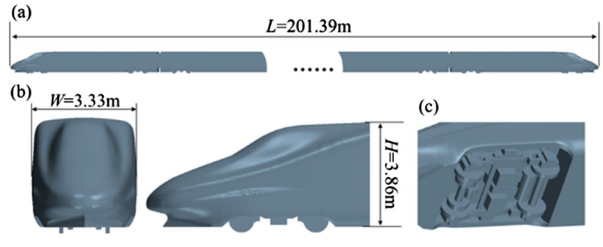

Figure 2. The model of the eight-marshalling train. (a) side view of the 8-marshalling Alpine HST, (b) the head car and (c) the bogie of the train.

study. The length, width, and height of the EC are $4W$, $0.98W$, and $0.22W$, respectively. The EC model includes two dust collection airboxes, a water tank, a transformer, and a converter as shown in Figure 3. The ventilation equipment of Alpine HST adopted the independent-air duct, the air inlet and outlet of the equipment connected by deflector shields and air duct. Besides, it contains fans installed inside the air duct, forcing the air to flow in and out from the equipment. A grille and filter are installed at each air vent to smooth the train surface and screen out impurities.

2.2. Numerical method

The IDDES approach, which has been validated to capture the flow fields around the train simulation (Cheng et al., 2022; Liang et al., 2020; Liu et al., 2022; Zhang, Adamu, et al., 2023), the wind-structure interaction simulation (Hu et al., 2018; Valger, 2022), the indoor ventilation simulation (Foster & Kinzel, 2021), and the wake flow investigation (Zhang, Gidado, et al., 2023; Zhang, Guo, et al., 2022; Zhang, Wang, et al., 2022), is used in the current study. In addition, the unsteady Reynolds-averaged Navier-Stokes (URANS) model and the IDDES are used to compare the results of the underbody flow state to LES (Dong et al., 2022). The results show that the minimum velocity discrepancy, between RANS (URANS) and LES is 14.4%. The similar difference between the LES and IDDES is 3.6%.

As a hybrid modelling approach, the basic principle of IDDES is to use the RANS resolution in the boundary layer to reduce the cost of near-wall resolving while preserving the fidelity of LES in the flow-separated region. For the RANS portion, the Shear-Stress Transport (SST) k-ω turbulence model is used for modelling as it is known to have better performance in adverse pressure gradient flows and free-stream independence (Shur et al., 2008). The continuity and momentum equations are discretized using the commercial finite volume solver STAR-CCM+. In particular, the hybrid upwind scheme is used for the discretization of convective fluxes to blend the second-order upwind scheme in RANS computations with the central differencing for LES. The second-order implicit scheme is used for the temporal advancement, and the time derivative discretization for unsteady flow calculations. The Semi-Implicit Method for Pressure-Linked Equations (SIMPLE) algorithm is used to update the pressure and velocity fields.

2.3. Computational domain and boundary conditions

In this paper, the ventilation simulation is divided into two steps. Firstly, the external field of 8-marshalling Alpine HST is simulated, to obtain the flow field around the EC near the head car and tail car of the train. Next, the velocity distribution on the inlet from the external-field simulation is input to the EC-area computational region and the EC-area simulation is performed. The computational domain and boundary conditions of two-step simulations are presented as follows.

2.3.1. External-field simulation

The calculation domain of the external-field simulation is shown in Figure 4(a), the height and width of the computational region are $11W$ and $21W$, which accounts for a blockage ratio of about 0.5%. The inlet is set at $11W$ upstream and the outlet is located at $31W$ downstream of the model. Besides, the ground clearance of the underbody is 0.2 m. For the boundary condition, the velocity inlet is given a uniform incoming flow with a speed of 55.56 m/s (U_{inf}), the Reynolds number $Re = 1.273 \times 10^7$ based on the width W of the train. The ground is set as a no-slip moving wall and given the same speed as the inlet. A zero static pressure is given at the pressure outlet. The lateral and upper walls are set as slip walls, and the surface of the train is set as a no-slip stationary wall.

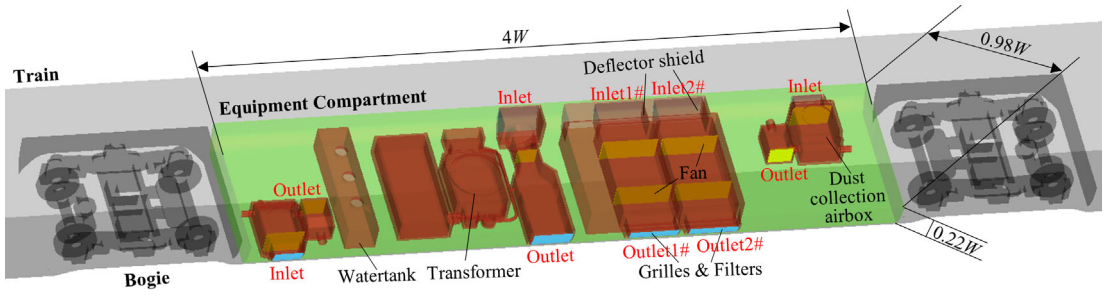

Figure 3. The model of the equipment compartment and electrical facilities.

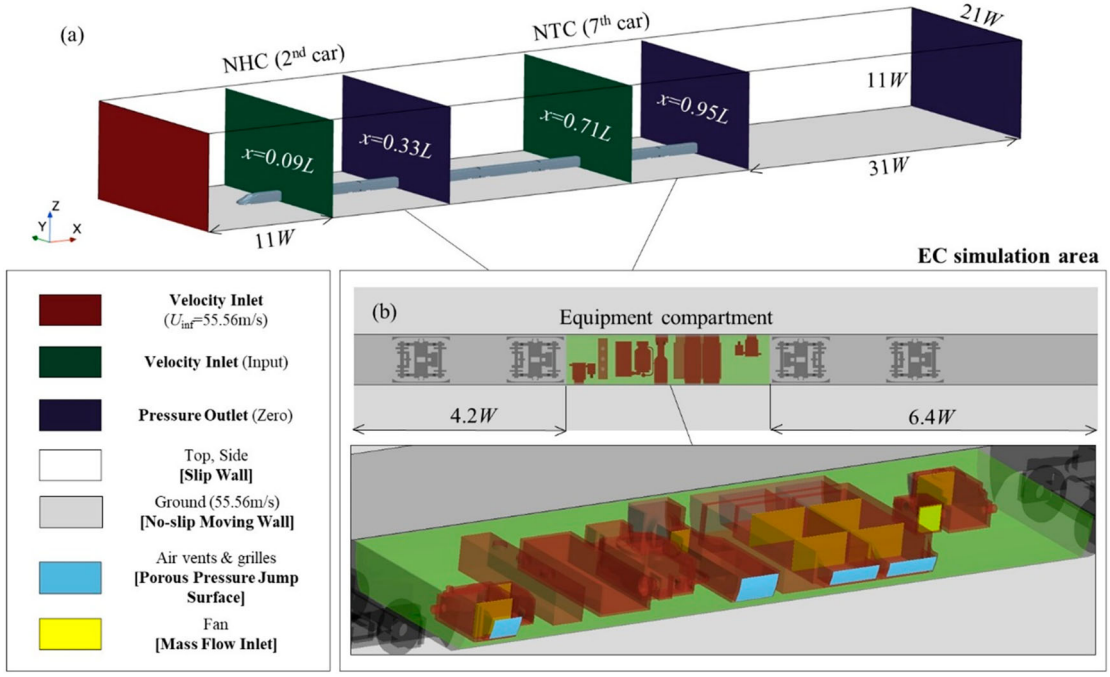

Figure 4. The calculation domain of (a) the external-field simulation and (b) the EC-area simulation.

2.3.2. EC-area simulation

The EC-area simulations of the 2nd car and 7th car are denoted as a near head car (NHC) and near tail car (NTC) condition. The calculation domain of the EC-area simulation is shown in Figure 4(b), the length of the computational region in the EC-area simulation is $15W$. The width ($21W$), height ($11W$) and ground clearance of the train are the same as the external-field simulation. For the NHC condition, the length region is from $x = 0.09L$ to $x = 0.33L$. For the NTC condition, the length region is from $x = 0.71L$ to $x = 0.95L$. The time-averaged velocity distributions on the inlet surface near the 2nd car and 7th car taken from the simulation results of the external-field simulation are applied as boundary conditions respectively. The velocity inlet of the NHC and NTC condition is obtained from the cross-section plane on $x = 0.09L$ and $x = 0.71L$, respectively. The lateral and upper walls are set as slip walls. A zero-pressure outlet is set as the boundary condition of the outlet end. The ground is a no-slip moving wall with a speed of 55.56 m/s. The fans mounted in the inlet and outlet of the air duct inside the dust collection airbox and converter, and the inlet of the transformer are set as mass flow inlet boundary conditions. The airflow direction of the fans in the inlet vent (denoted as extractor fan) is from the external environment to the air duct, and the direction of the fans in the outlet vent (denoted as exhaust fan) is from the air duct to the external environment. The specific parameters are listed in Table 1. The grilles and filter are simplified as porous pressure jump surfaces in this simulation, and the pressure loss caused by them is calculated according to Eq. (1) (Cheng et al., 2008).

Table 1. The rated working parameters of the ventilation equipment (Zhang, 2007).

Equipment		Mass flow rate/(kg/s)
Dust collection air box	Inlet	1.8375
	Outlet	1.021
Transformer	Inlet	3.0625
Converter	Inlet	1.3271
	Outlet	0.79625

$$\Delta P = \alpha \cdot \rho |v|^2 + \beta \cdot \rho |v| \tag{1}$$

where ΔP is the pressure loss (Pa), ρ is the air density, 1.225 kg/m^3, and v is airflow velocity (m/s), α is the porous inertial resistance and β is the porous viscous resistance. Here, the α is equal to 0.42996 and β is equal to 4.27159.

2.4. Mesh strategy

2.4.1. External-field simulation

The trimming and prism layer mesh methods are used. The first layer thickness is 0.37 mm with a growth factor of 1.2, and 12 prism layers are produced to solve the boundary on the wall surface. The average surface mesh sizes of the bogies and train are 0.0296 and 0.0592 m, as shown in Figure 5. The overall number of computational cells is 26.3 million. The normalised time step is $\Delta t = 5 \times 10^{-4} s$, which ensures the CFL number is lower than 1

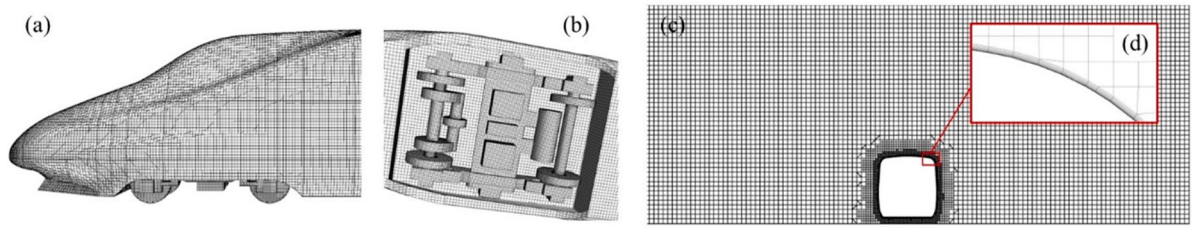

Figure 5. The grid construction of (a) the train, (b) the bogie, (c) the computational region and (d) the prism layers.

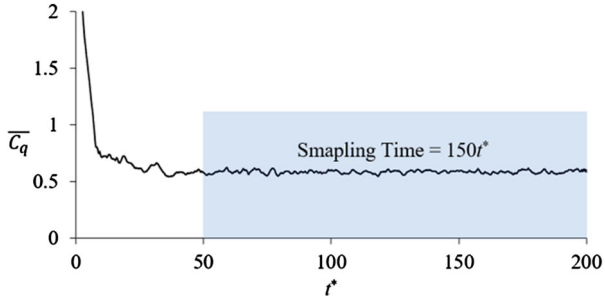

Figure 6. The time-averaged pressure coefficient of the train as a function of the dimensionless time t^*.

in around 99% of the cells in the interest region. After a characteristic time, $t* = tU_{\text{inf}}/W = 50$, which is about 1 time for the air passing the entire computational region of the external-field simulation at free-stream velocity, the airflow velocity becomes dynamically stable with the residual of the cp of the train below 10^3 for each time step. To ensure that the flow is fully developed, the total computational time is $t = 200t^* = 12$s, which is about 3 times for air passing the entire computational region of the external-field simulation at free-stream velocity, as shown in Figure 6.

2.4.2. EC-area Simulation

The same mesh method as the external-field simulation is used, and the first layer thickness of 0.21 mm and 12 prism layers are applied. The refinement areas are set around the equipment and cabin as shown in Figure 7. The average value of wall y + on the train and the EC surfaces are lower than 10, and the equipment surfaces are lower than 30, which satisfies the requirement of the target wall $y+$ value is $1 < y+ < 30$ based on the IDDES model with hybrid wall functions. The physical time step of the transient calculation is $\Delta t = 5 \times 10^{-4}s$, which ensures the CFL number is lower than 1 in around 99% of cells in the interest region. The maximum number of inner iterations for each time step is 10. After a characteristic time, $t^* = tU_{\text{inf}}/W = 15$, which is about 1 time for the air passing the entire computational region of the EC-area simulation at free-stream velocity, the airflow velocity becomes dynamically stable with the residual of the cp of each electrical facility below 10^3 for each time step. To ensure that the flow is fully developed, the total computational time is $t = 45t^* = 2.7$s, which is about 3 times for air passing the entire computational region of the external-field simulation at free-stream velocity, as shown in Figure 8.

To test the mesh sensitivity, three mesh cases were generated on the EC-area simulation region, with the mesh details as in Table 2. A profile ($z = 0.74$ m) in the middle of the EC in the z-direction is created. The time-averaged pressure coefficient in three mesh cases near the inlet and outlet vent of the EC in the $z = 0.74$ m plane is shown in Figure 9. The centre of the dust collection air box (DCAB1# and DCAB2#), transformer and converter (AD1# and AD2#) are denoted as a, d, b, c_1 and c_2, respectively. The points at $y = 0.68W$ and $y = -0.68W$ were selected as the pressure coefficient monitoring points for the inlet and outlet vent, respectively. By comparing the C_p near the vents of the five points between three mesh cases, the coarse mesh has a significant deviation from the others. The largest deviation between medium and fine mesh occurs at the outlet of c_2, at around 7%. Thus, the medium mesh case is deemed to meet the grid independence requirements, and is used for the subsequent simulations.

3. Results and discussion

3.1. Method validation

3.1.1. Numerical method validation

Since it is hard to perform wind tunnel measurements of airflow velocities in the EC, the results of wind tunnel experiments with airflow measurements around a cube building (with open doors in both windward and leeward walls) (Jiang et al., 2003) are compared with the IDDES simulation, to verify the accuracy of the airflow simulation method in this paper. The geometry model and the comparison result are shown in Figure 10. The building model is a cube of 250 mm edge length. The dimensions of the opening doors are 84 mm × 125 mm (length × height), and the thickness of the wall is 6 mm. The maximum wind speed in the wind tunnel is 12 m/s.

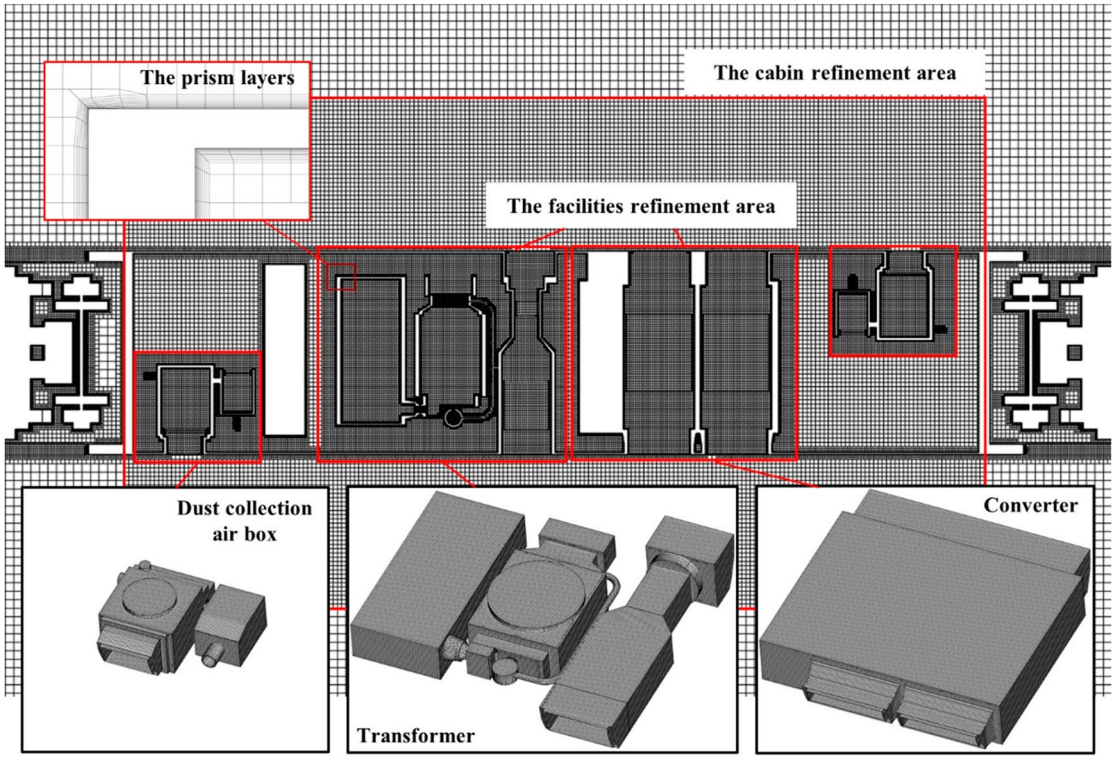

Figure 7. The grid construction details of the EC and electrical facilities.

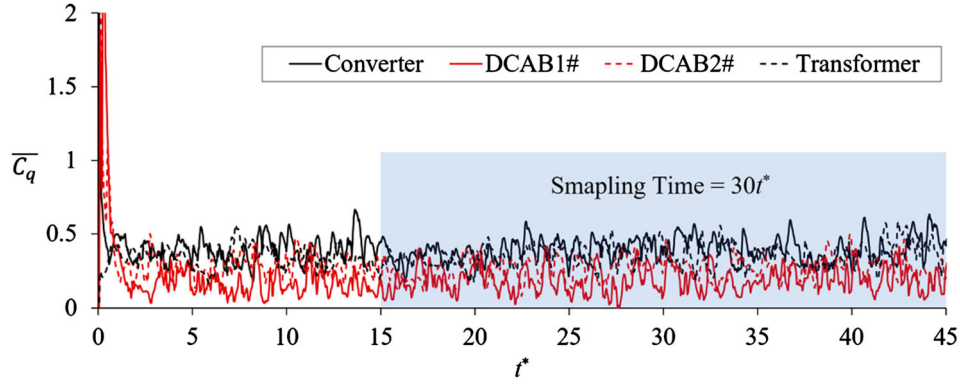

Figure 8. The time-averaged pressure coefficient of electrical facilities as a function of the dimensionless time t^*.

The airflow velocity is measured by the anemometer with a one-dimensional LDA system, which can measure the airflow speed in both horizontal and vertical directions. All the test points are arranged in the centre section of the building. The computational domain is established with a height of 4 h (h is the edge length, 250 mm) a width of 4 h along both sides of the domain, and the length of upstream and downstream 4 and 8 h, respectively. The measurement points are arranged in the planes near the entrance ($-0.04\,h$) and the exit ($1.5\,h$) of the building, as shown in Figure 10(a).

The trimming and prism layer mesh methods are used, and the first layer thickness of 0.153 mm and 15 prism layers are applied. The average surface mesh size of the building is 0.0306 m. The overall number of computational cells is 4.12 million. The physical time step of the transient calculation is $\Delta t = 2.5 \times 10^{-4} s$, which ensures the CFL number is lower than 1 in around 99% of cells

Table 2. The details of the EC-area simulation in three mesh cases.

	Mesh size/m		
Mesh details	Coarse	Medium	Fine
The equipment surface	0.0336	0.0168	0.0084
The equipment refinement area	0.0672	0.0336	0.0168
The cabin refinement area	0.1344	0.0672	0.0336
Total cells/($\times 10^7$)	0.54	2.15	8.93

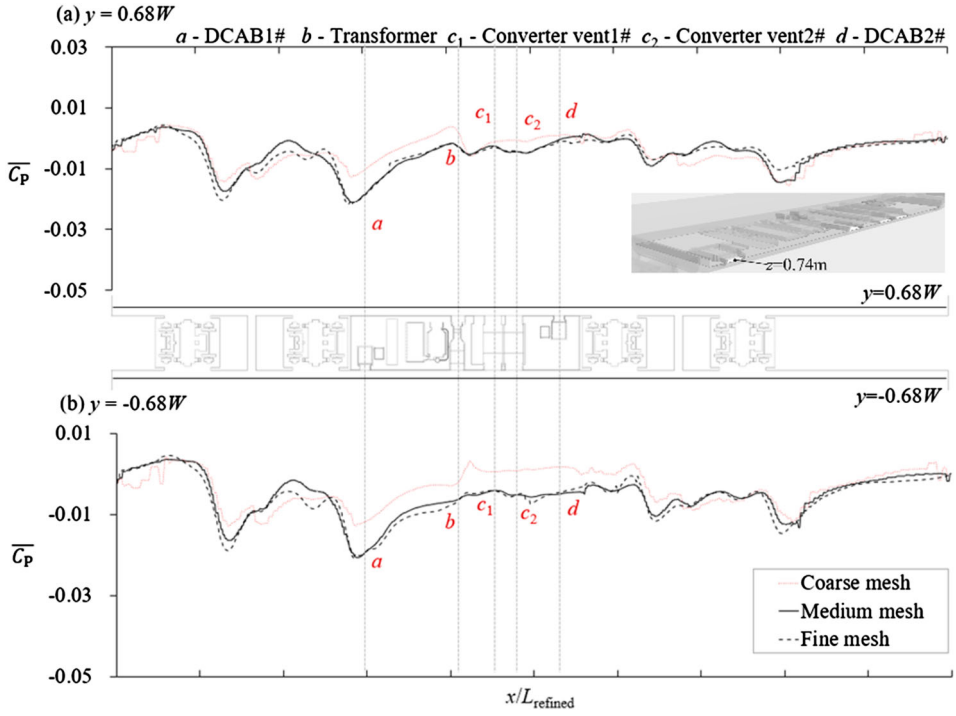

Figure 9. The time-averaged pressure coefficient in three mesh cases near (a) the inlet and (b) the outlet vent of the EC in the $z = 0.74$ m plane.

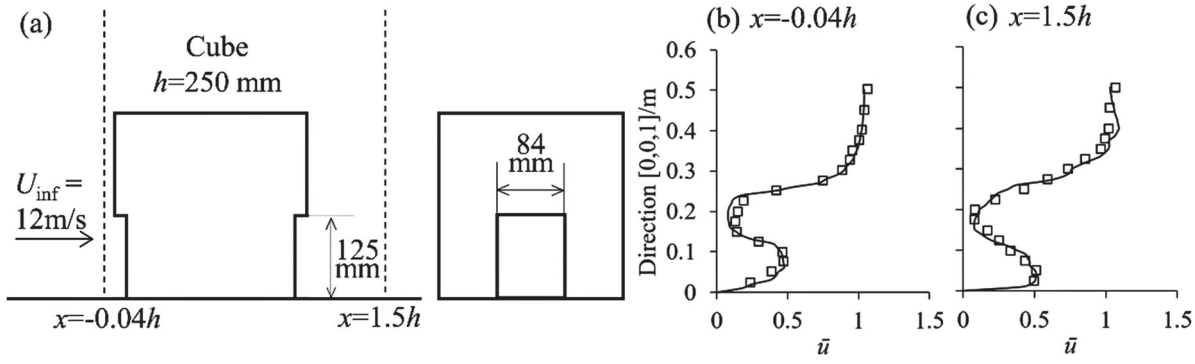

Figure 10. (a) The geometry model of the cube building and u velocity comparison of (b) $x = -0.04\,h$ and (c) $x = 1.5\,h$.

in the interest region. The maximum number of inner iterations for each time step is 10. After a characteristic time, $t^* = tU_{\text{inf}}/h = 6$ when the airflow velocity becomes dynamically stable, the data begins sampling and averaging results for a $t*$ of 18.

The comparison of u velocity between the wind tunnel test and simulation is shown in Figure 10(b) and (c). The numerical prediction is close to the velocity measured in the experiment, with a maximum error of around 5%. Therefore, the results of the numerical calculation can be considered sufficiently accurate.

3.1.2. Two-step simulation method validation

To verify the EC-area simulation is practicable and efficient, a combined simulation of the whole 8-marshalling train and two ECs in the 2nd car and 7th car is conducted, as shown in Figure 11. In the combined simulation, the same boundary conditions and mesh strategy are used in the external-field simulation and the EC-area simulation. The height and width of the computational region are $11W$ and $21W$. The inlet is set at $11W$ upstream and the outlet is located at $31W$ downstream of the model. Besides, the ground clearance of the underbody is 0.2 m. For the boundary condition, the velocity inlet is given a uniform incoming flow with a speed of 55.56 m/s (U_{inf}). The ground is set as a no-slip moving wall and given the same speed as the inlet. A zero static pressure is given at the pressure outlet. The lateral and upper walls are set as slip walls, and the surface of the train is set as a no-slip stationary wall. The interfaces of fan are set as mass

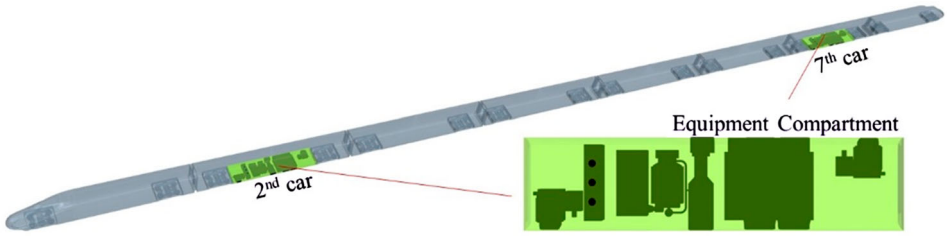

Figure 11. The combined model of the 8-marshalling train and two ECs.

flow inlets. The grilles and filter are simplified as porous pressure jump surfaces in this simulation.

The trimming and prism layer mesh methods are used, and the first layer thickness of 0.21 mm and 12 prism layers are applied. The average surface mesh sizes of the electrical facilities, bogies, and train are 0.0168, 0.0168, and 0.0336 m, respectively. The overall number of computational cells is 91.7 million. The normalised time step is $\Delta t = 5 \times 10^{-4} s$, which ensures the CFL number is lower than 1 in around 99% of the cells in the interest region. The transient simulation begins sampling and averaging for the period of $t^* = tU_{\text{inf}}/W = 100$, after the initial period of $t^* = 50$ when the flow field becomes dynamically stable.

The time-averaged pressure coefficient of two kinds of simulation methods near the inlet and outlet vents of EC are shown in Figure 12. It can be observed that the pressure coefficient of the two methods has similar fluctuation and values. The CPU solver time per time-step of the combined simulation and the EC-area simulation is 3.05 and 1.16 h which is reduced by 62%. The total computational times of the two simulation methods are about 203 and 75 h with 192 cores.

3.2. Velocity inlet boundary characteristic

The time-average velocity magnitude $\mathfrak{V}$ distributions (normalised by U_{inf}) on the inlet surface near the head and tail car from the simulation results of the external-field simulation are shown in Figure 13. The width of the low-speed area ($0.99U_{\text{inf}}$) on the inlet boundary in the NHC condition is 3.67 m and it is increased to 5.92 m in the NTC condition, which becomes 61% wider. The velocity distribution of the inlet boundary in the NHC condition is characterised by a 'w' shaped with two high-speed disturbances (a_1 and a_3) on both sides of the train and two low-speed disturbances near two wheels area at the bottom of the train (a_2 and a_4), while in the NTC condition, the velocity distribution is characterised by a 'u' shaped with one low-velocity disturbance (b_2) and two high-speed disturbances (b_1 and b_3) which are relatively far away from the sides of the train.

3.3. Ventilation characteristic

First, the external field around the EC is analysed. The time-averaged velocity contours in the $z = 0.74$ m plane are presented in Figure 14. The outermost black line is the location of the low-speed boundary layer ($v = 0.99U_{\text{inf}}$) around the EC. The low-speed layer near the tail car is significantly thicker than that of the EC near the head car. A small boundary layers' thickness variation (from $0.99U_{\text{inf}}$ to 0) corresponds to a large velocity gradient, which makes it hard for the airflow to be drawn into or to be exhausted from the EC. In the NHC condition, the EC area has a smaller gradient of velocity variation than the two ends of the bogies area. In the NTC condition, the velocity gradient variation is greater in the EC area, especially around the outlet of the EC.

To further analyse the situation of the external airflow into the EC, the distributions of the time-averaged u velocity in the $z = 0.74$ m plane are shown in Figure 15. The black lines inside the EC are the locations of the ventilation fans installed in the air duct (AD) of the electrical facilities, which guides the airflow towards the negative y-direction. Blue arrows indicate the airflow into the EC, and red arrows are the reverse. As the train operates, the external airflow is drawn into the equipment by the combined effect of the pressure difference between the inside and outside of the EC and the ventilation fans. The path of the airflow into the AD is close to the wall on the windward side. With the resistance effect of the wall, two high-velocity airflows appear along the wall and toward the centre of the AD. In addition, under the action of the fans, the positive airflows from the outlet vent are squeezed and discharged to the external environment along the leeward wall of the AD. A comparison of the variation in y-velocity at the different air vents is shown in Figure 15. The deviation rate of the velocity is defined here as $R_v = (v_{\text{NTC}} - v_{\text{NHC}})/v_{\text{NHC}}$. To observe the detailed trends of airflow velocity near the vents, the points at $y = 0.526W$ and $y = -0.526W$ are selected as the monitoring points for the inlet and outlet vents. Near the inlet vents of the facilities (Figure 16(a)), the airflow velocity is smaller in the NTC condition than that in the NHC condition. The airflow velocity at the inlet of the

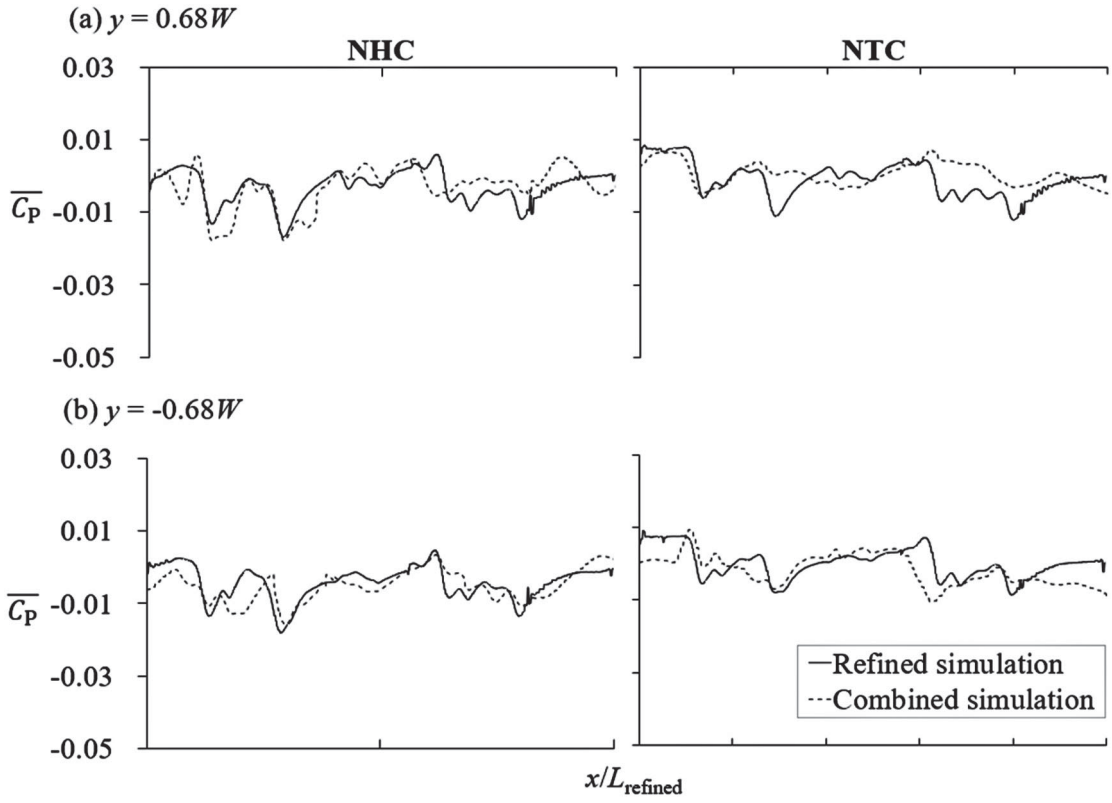

Figure 12. The time-averaged pressure coefficient of two kinds of simulation methods near the (a) inlet and (b) outlet vents of EC.

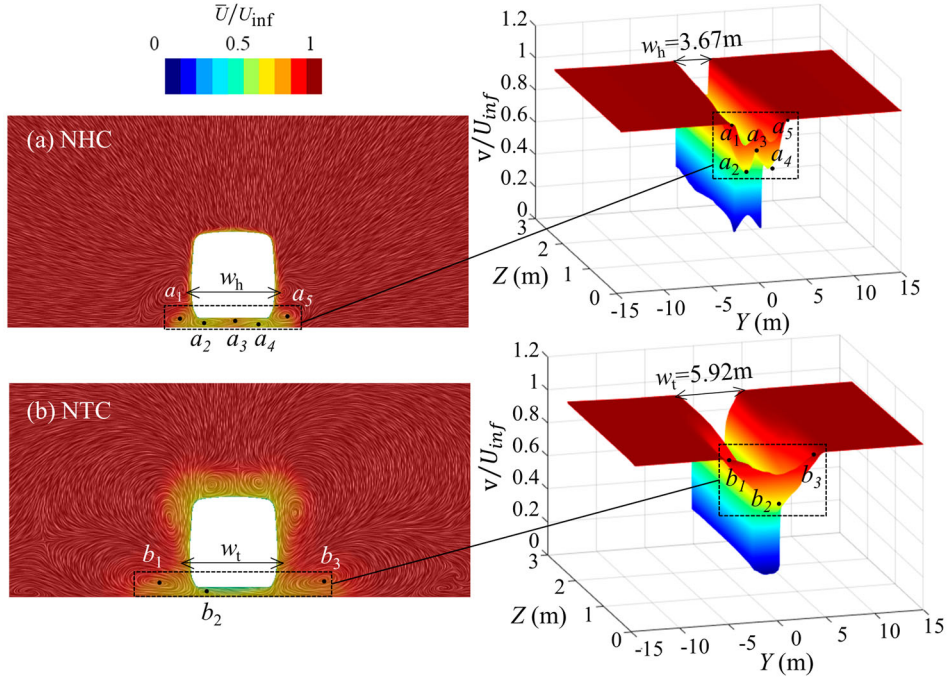

Figure 13. The input-velocity boundary condition of the inlet from the external-field simulation. (a) near head car condition and (b) near tail car condition.

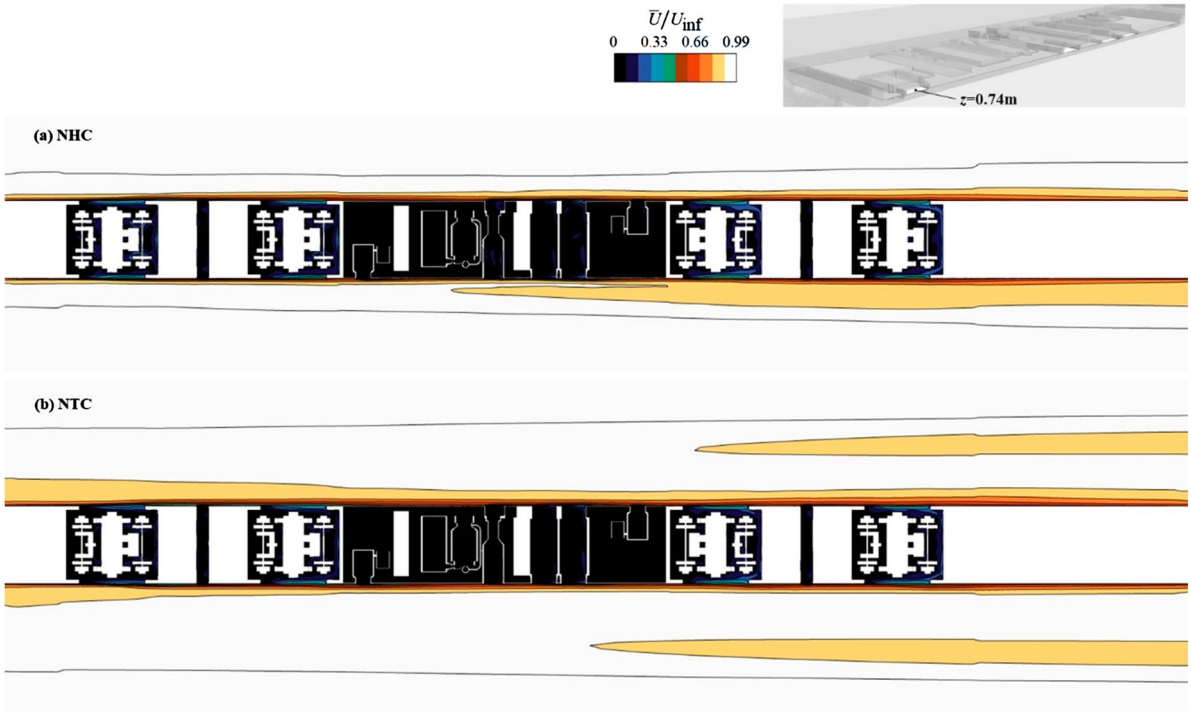

Figure 14. The time-averaged velocity contour of the EC in the $z = 0.74$ m plane in (a) near head car and (b) near tail car conditions.

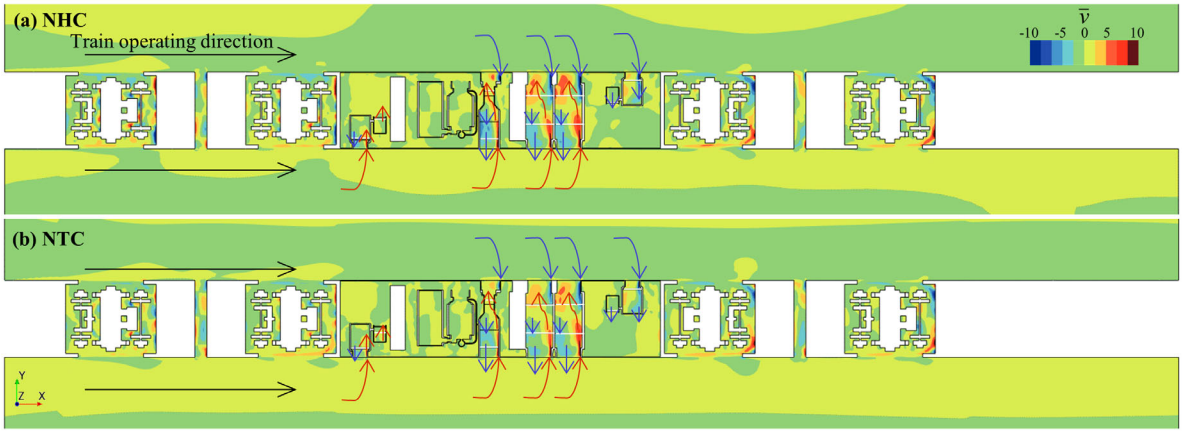

Figure 15. The time-averaged v velocity distribution of the EC in the z = 0.74 m plane in (a) near head car and (b) near tail car condition.

DCAB2# is greatly influenced by the location of the EC, with an inhibition ratio R_v of −63%. Near the outlet vents of the facilities (Figure 16(b)), the airflow velocity in the front half of the EC in the NTC condition is greater, while the rear half is smaller than that in the NHC condition. The turning point is between the two ADs of the converter. The airflow velocity at the converter outlet1# is greatly influenced by the location of the EC, with a promotion ratio R_v of 51%. It was therefore found that the vents close to the rear bogie will be greatly affected by the location of the EC. To explain it, the time-averaged pressure coefficient distribution of the EC is presented in Figure 17. As is clear in the figure, the gradient of pressure variations between the external environment and the interior of the EC in the NHC condition is significant, which helps the airflow exchange. In contrast, the pressure gradient is not obvious in the NTC condition. Moreover, the closer the bogie, the greater the pressure distribution is influenced by the location of the EC.

Next, the ventilation characteristic of the AD inside the electrical facilities is further analysed. The following analysis is based on the two air ducts of the converter, since it has a relatively regular shape of ADs. As Figure 18, Fan1# is an extractor fan mounted at the inlet vent of the converter to draw the air from the outside environment into the AD, and Fan2# is an exhaust fan at the outlet vent to discharge the air to the outside. Based on the installation position and working characteristics of the fan, it is

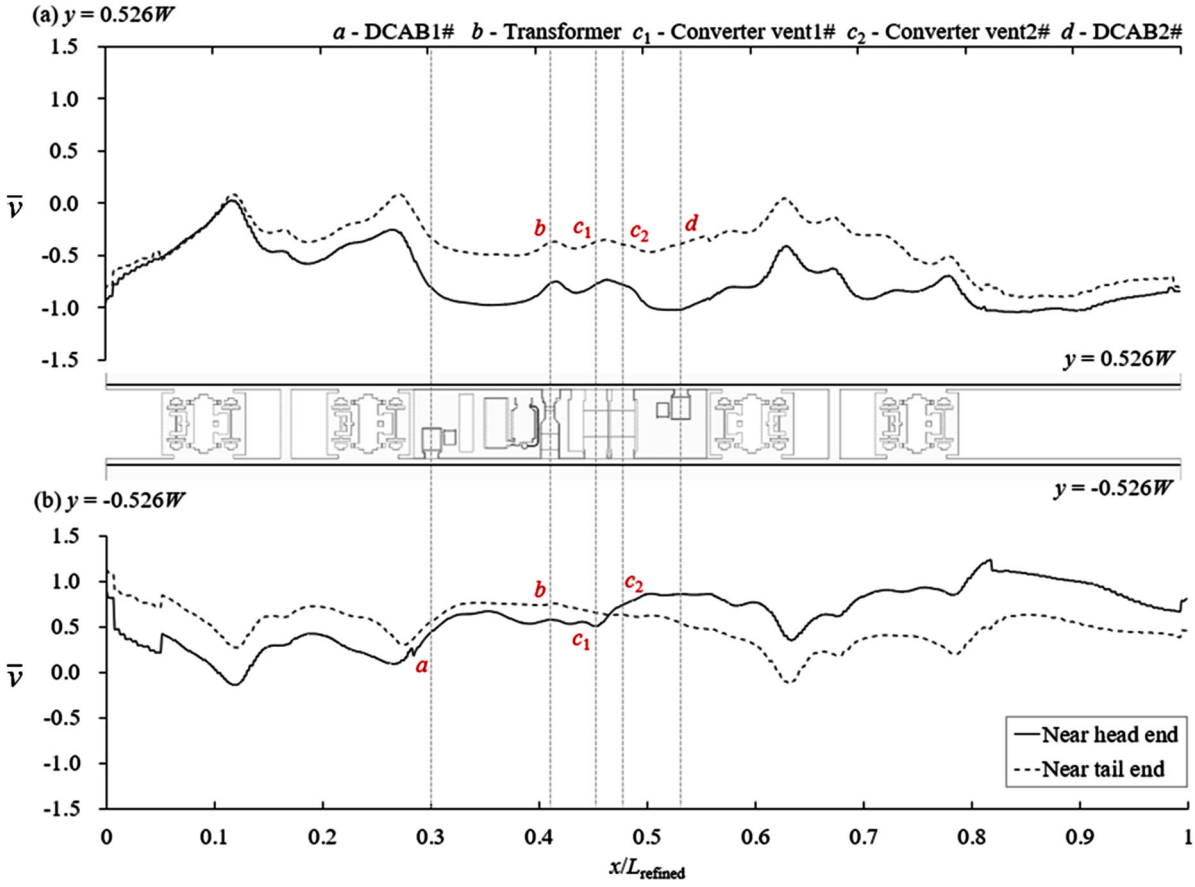

Figure 16. The time-averaged *v* velocity in two conditions near (a) the inlet and (b) the outlet vent of the EC in the $z = 0.74$ m plane.

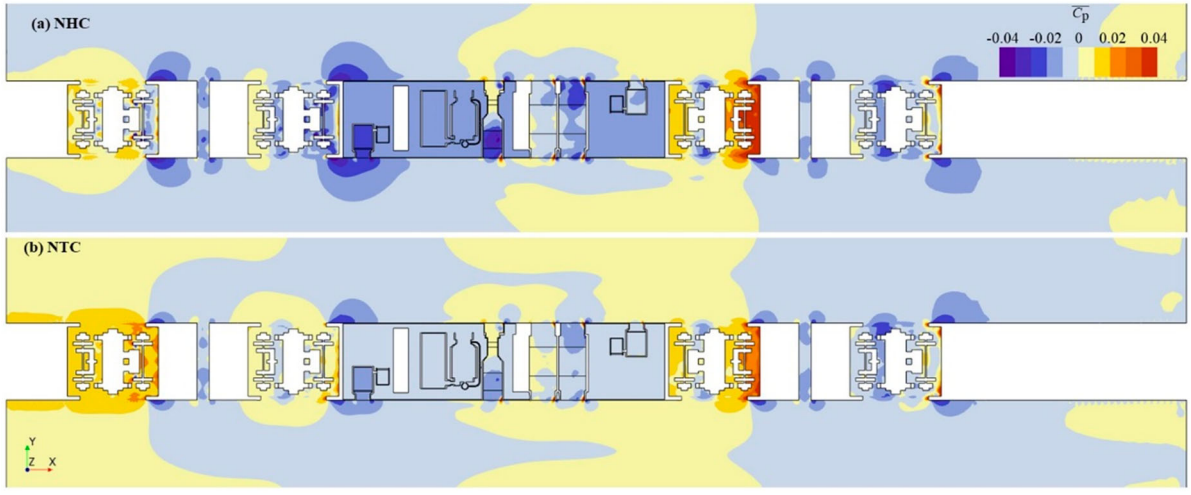

Figure 17. The time-averaged pressure coefficient distribution of the EC in the $z = 0.74$ m plane in (a) near head car and (b) near tail car conditions.

presumed that the pressure distribution conducive to the normal operation of the fan should have a higher positive pressure or a lower negative pressure near the inlet ($y_1 = 0.26W$) and a lower positive pressure or a higher negative pressure near the outlet ($y_2 = -0.26W$). However, the corresponding pressure distribution front and rear of the fan in Figure 18(a,b) shows that the operation of the extractor fan is inhibited and the exhaust fan could work at a lower load. To explain this, the airflow in the AD is pushed towards the external environment, due to the greater negative pressure outside the inlet and outlet vent. Leave aside the working condition of the fan, a significant

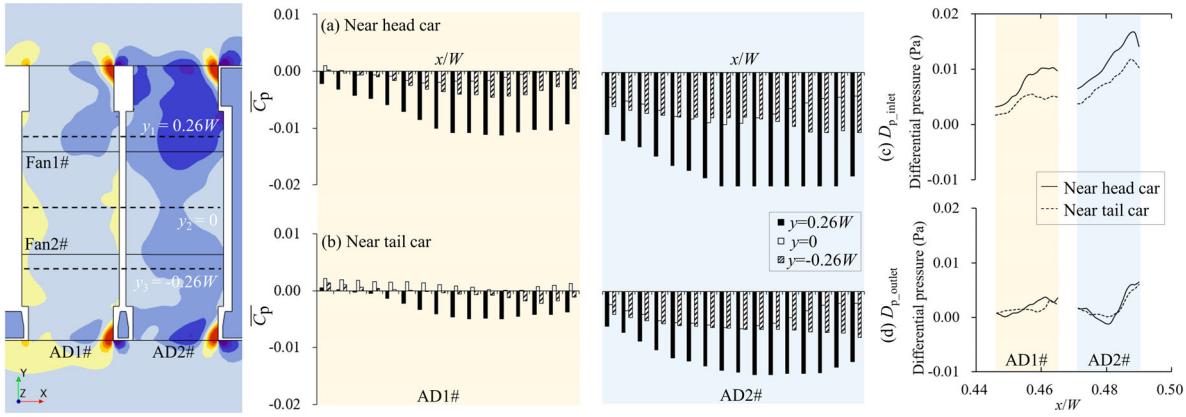

Figure 18. The time-averaged pressure coefficient distribution inside the AD in (a) NHC and (b) the NTC conditions, (c) the differential pressure between the fore and rear of the fan in the inlet and (d) the outlet vents.

differential pressure between the outside environment and the inside of the AD can promote the equipment ventilation performance. Define the differential pressure between the fore and rear of the fan inside the AD in the inlet end $D_{p\_inlet} = C_{p\_y2} - C_{p\_y1}$ and the outlet end $D_{p\_outlet} = C_{p\_y2} - C_{p\_y3}$. As shown in Figure 18(c,d), it has a larger undulating differential pressure in the inlet end and it is a gentle variation in the outlet end. Compared to the NTC condition, the ADs near the head car have greater pressure variations. In addition, the adjacent vents have different pressure distributions. The pressure variations at the AD2# are greater than the AD1#. Correspondingly, the larger velocity areas occur in the vents in the NHC condition. The inlet2# in the NHC condition has the largest area of airflow toward the external environment, as shown in Figure 19. Overall, for the converter in the same EC, the ventilation performance of the AD2# is more favourable. For the different locations of the EC, the ventilation performance is preferred in the NHC condition.

Two yz-profiles ($x_1 = 0.46L_{refiend}$ and $x_2 = 0.48L_{refiend}$) in the middle of two ADs of the converter are created. The motion of the airflow inside the ADs is analysed by visualising the in-plane velocity vector image in the x_1 and x_2 profiles of the ducts (Figure 20). Due to the abrupt shape change between the duct and the vent, the direction of the airflow is altered (as shown by the red arrows). This makes it difficult for the extractor fan (grey line), at the rear of this abrupt change, to draw the air into the duct. After the rectification by the duct, the exhaust fan (black line) can easily discharge the airflow out to the external. Part of the airflow is, blocked by the abrupt change of the outlet end at the rear, creating a backflow. It can be observed that after the airflow meets the shape mutations, it would rotate in two directions, as shown in Figure 21. The positive vorticity near the shape mutation of the inlet end area dominates, while the negative vorticity is dominant near the outlet end. Moreover, strong vorticity sheets are observed at the inlet and outlet vents in the NHC condition (Figure 21(a,b)). The closer to the

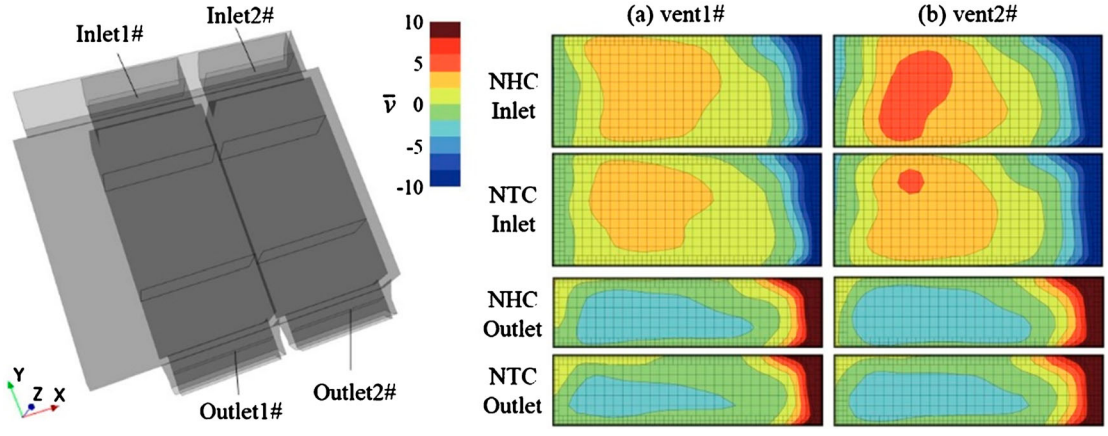

Figure 19. The time-averaged v velocity distribution of (a) vent1# and (b) vent2# near inlet and outlet vents in NHC and NTC conditions.

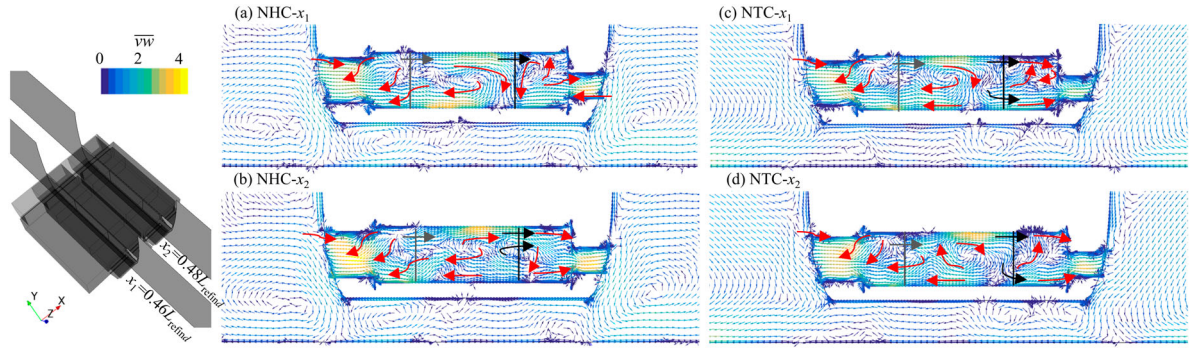

Figure 20. The time-averaged in-plane velocity vector image of the ADs in the *yz*-profile in (a) AD1#, (b) AD2# of NHC and (c) AD1#, (d) AD2# of NTC condition.

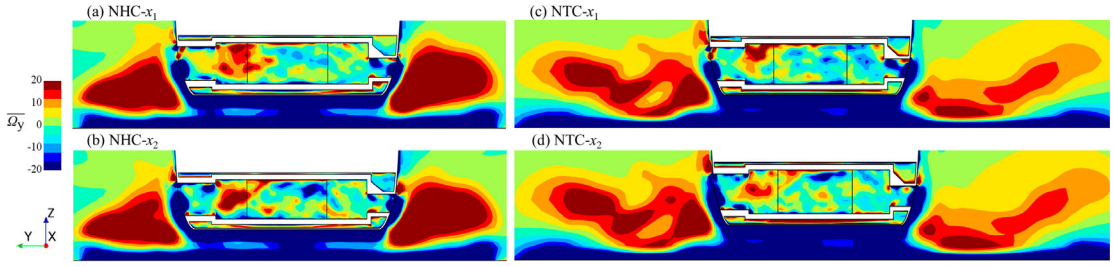

Figure 21. The time-averaged *v* vorticity contours of the ADs in the *yz*-profile in (a) AD1#, (b) AD2# of NHC and (c) AD1#, (d) AD2# of NTC condition.

EC of the tail car, the vortices on two sides of the vents gradually dissipate to the sides.

4. Vehicle experiment on ventilation measurement

In the real-vehicle tracking test, the Alpine HST was operating between Urumqi-Hami-Lanzhou with a total length of 1776 kilometres in north-western China, where the differential temperature in day-night is so extreme that the ventilation issue for the equipment become more serious. In such a special operating environment, critical electrical facilities are operating under a heavy load, which is often alerted due to high temperatures. Therefore, a real-vehicle tracking test can contribute to monitoring the ventilation performance of electrical facilities. The basic situation of the test is listed in Table 3. The converter in the 2nd car is selected for the measurement subject in this test. The measurement points are arranged at the outlet, due to the shape of the air inlet being irregular. As the train changed the running direction during the test, the relative location of the measurement subject was changed. When the train operates away from Urumqi, the 8th car will be the head car, and the measurement subject will be close to the tail car at this time (NTC condition), while the train approaches Urumqi, the 1st car is the head car, and the measurement subject will be close to the head car at this time (NHC condition).

4.1. Measurement method

A double heads T-type Pitot tube (TTPT) is developed by the Key Laboratory of Traffic Safety on Track (Central South University) (Xu et al., 2014). It is a symmetrical structure to meet the bi-directional flow measurement in the vehicle test, and its tubes are flexible to fit with the limited mounting space. The Chebyshev method is a common method of airflow measuring points arrangement. It requires that if the aspect ratio of the measurement section is > 1, there should be more than 5 lateral measurement points in each line (Caré et al., 2014). In this case, the aspect ratio of the measurement section is equal to $1000/240 = 4.167$, requiring 8 probes pre-line and 6 probes pre-column to be evenly arranged in the measurement section. Considering the limited space in the vent, the number of measurement points has been reduced to 4×2 points located in the middle area of the vent to leave enough space for ventilation, as shown in Figure 22.

The TTPT is connected to a differential pressure sensor using pressure transmission. According to the Bernoulli equation, the relationship of the differential pressure between two pressure holes of TTPT and the airflow velocity is given in Equation (2):

$$\Delta P_{\mathrm{d}} = \frac{1}{2}\rho v^2 \tag{2}$$

Table 3. The introduction of the real-vehicle test.

	Train traction mode	Marshalling quantity	Location of tested-converter	Train speed
Alpine HST	Power distribution Running routes	Eight-marshalling	2nd car Running mileage	200 km/h Test cycle
Alpine HST	Urumqi-Hami (NTC) Hami-Urumqi (NHC)	Urumqi-Lanzhou (NTC) Lanzhou-Urumqi (NHC)	1776 km	02/06/2016–12/10/2016

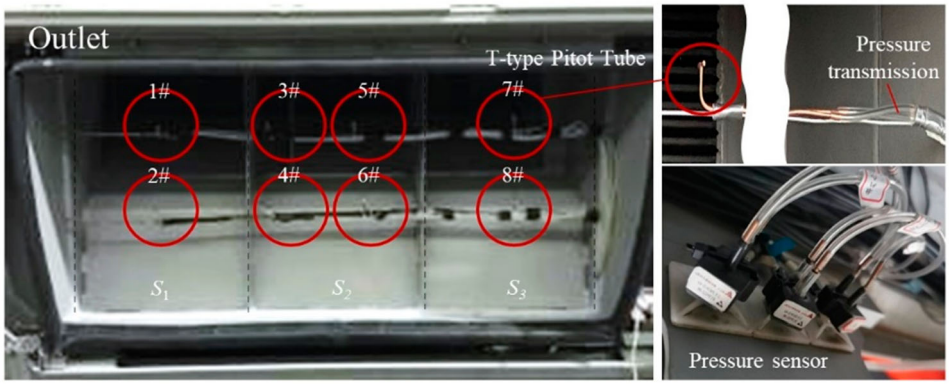

Figure 22. TTPT test system diagram

where ΔP_d is the dynamic pressure (Pa), ρ is the air density, 1.225 kg/m^3, and v is airflow velocity (m/s).

The air volume Q at the outlet vent cross-section is obtained:

$$Q = \frac{(v_{1\#} + v_{2\#})}{2} \cdot S_1 + \frac{(v_{3\#} + v_{4\#} + v_{5\#} + v_{6\#})}{4} \cdot S_2 + \frac{(v_{7\#} + v_{8\#})}{2} \cdot S_3 \quad (3)$$

where v is the average velocity of each measurement point and S is the area of the air outlet vent cross-section.

For comparing the air volume of the simulation and the real-vehicle test, they are normalised as in Equations (4) and (5).

$$c_{q\_sim} = \frac{Q_r}{Q_{rated}} \quad (4)$$

$$c_{q\_test} = \frac{Q_r}{Q_{rated}} / \frac{Q_{static}}{Q_{rated}} = \frac{Q_r}{Q_{static}} \quad (5)$$

where the air volume during the train in static (fans are working), operation, and the rated air volume of the ventilation equipment's cooling fan is denoted as Q_{static}, Q_r, and Q_{rated}, respectively. Different from the test, the Q_r of the simulation is obtained from the integration of the airflow velocity and the area of each cell grid.

4.2. Measurement correction

In the vehicle test, some wires were anchored inside the deflector shield of the converter's outlet vent, and the T-type Pitot tubes (TTPT) were fixed on the wires. The wires and the TTPT would increase the blockage ratio of the air outlet vent, which might affect the accuracy of the flow rate measurement. Hence, using the numerical calculation to compare the blockage effect of the Chebyshev method and the test measuring method described above, three different degrees of blockage were modelled as in Figure 23. The black lines show the vent grilles and the yellow lines show the fixed wires and TTPTs, with a width of 10 mm.

The blocking ratio B

$$B = \left(S - \sum_{i=1,j=1}^{ij} s_{ij} \right) / S \quad (6)$$

where S is the total area of 0.240m^2, and the area $\sum_{i=1,j=1}^{ij} s_{ij}$ is the effective ventilation area.

Hence, the effective areas of three different blockage degrees are 0.2352, 0.2167and 0.1862 m^2, corresponding to the blocking ratio are 2.0%, 9.7%, and 22.4%, respectively.

According to the simulation result in Figure 24, the blockage effect of the test measurement method on the ventilation is not so obvious that the air volume deviation from the original model is around 2%, while the deviation from the Chebyshev measurement method is around 4%.

Since the test measurement method is a non-standard method, the measuring value needs to be corrected based on the Chebyshev method. A correction factor c is defined, and the average correction factor $c_v = 0.882$ will

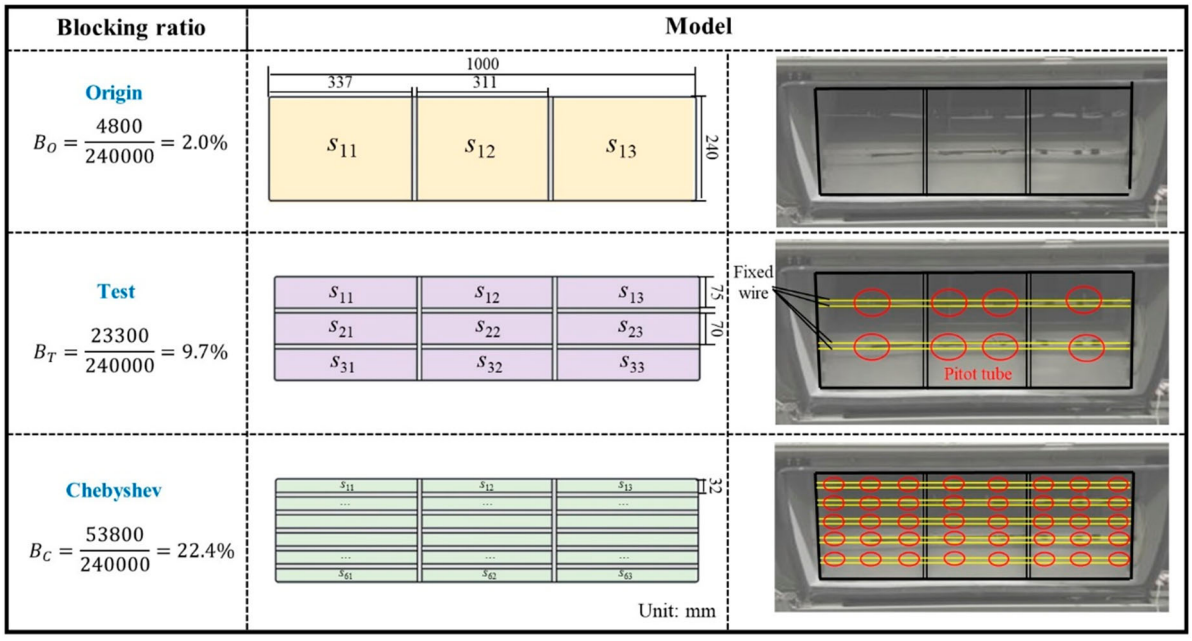

Figure 23. The model of the three different blockage ventilation equipment outlets.

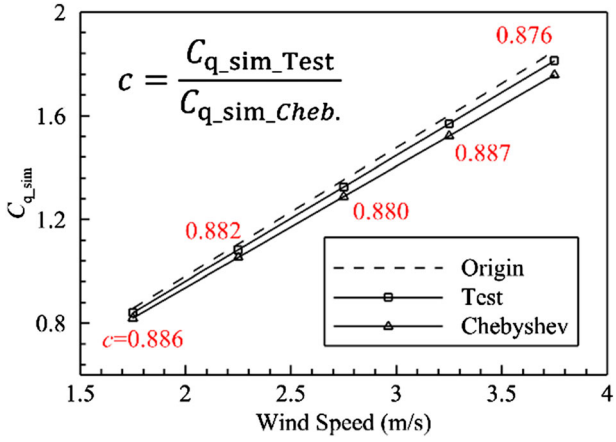

Figure 24. The air volume of different blockage models under different wind speeds.

be used in the data processing of the vehicle test to reduce the deviation due to fewer measuring probes in the test.

4.3. Results analysis on running location

The air volume of different running locations in different operating routes during the test cycle is shown in Figure 25.

The test data during the single-train operation in different directions were picked out according to the operating mileage logs. In static conditions, the averaged air volumes of the air outlet when the train runs on the route Urumqi-Hami and Urumqi-Lanzhou are 4580 and 4304 m^3/h, respectively, which are higher than the rated air volume of 3900m^3/h to meet the normal working requirements of the equipment.

When the train is running at full speed 200 km/h, the operating direction has a great impact on the air volume. In NHC conditions of Hami-Urumqi and Lanzhou-Urumqi, the average air volumes are 4940 and 4409m^3/h, which is 7.9% and 2.4% higher than the static air volume, respectively. In NTC conditions of Urumqi-Hami and Urumqi-Lanzhou, the average air volumes are 3828 and 3822 m^3/h, in other words, which is close to or even lower than the rated air volume of 3900 m^3/h. Compared to the static air volume, the restraint ratios are −16.4% and −11.2%, respectively.

4.4. Results comparison between simulation and test

Comparing the air-volume coefficient of the outlet vent 1# between the vehicle test and the EC-area simulation in Table 4. Define an inhibition ratio to reflect the difference between the NHC and NTC condition, $R_i = (c_{q\_tail} - c_{q\_head})/c_{q\_head}$, and a deviation ratio reflected the difference of the simulation and test, $R_d = (c_{q\_test} - c_{q\_sim})/c_{q\_sim}$. It is the same that the air volume in NHC condition is being promoted while in NTC condition is being inhibited. The values measured in the test seem to magnify the difference between the NTC and NHC conditions. The inhibition ratios of the test and simulation conditions are −22.5% and −26.3%. This factor is not taken into account in the NTC simulation in this paper. Nevertheless, the deviation ratios between the test and simulation in the NTC and NHC conditions are −8% and −4%. Therefore, the measurement method in this study is relatively reliable.

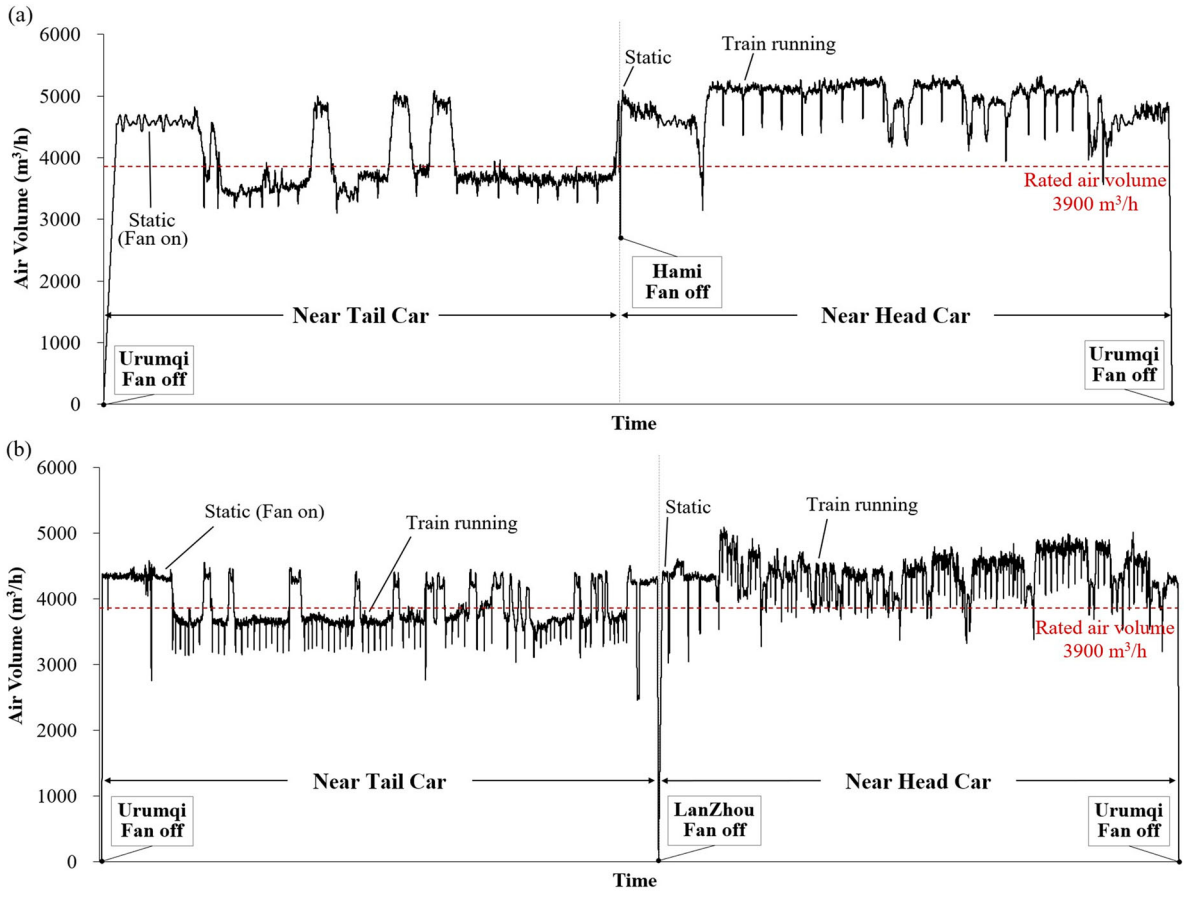

Figure 25. The air volume of different running directions in (a) the Urumqi-Hami running route and (b) the Urumqi-Lanzhou running route.

Table 4. The comparison of the normalised air-volume coefficient between simulation and test.

	Near Tail Car	Near Head Car	Inhibition ratio $\frac{(c_{q\_tail}-c_{q\_head})}{c_{q\_head}}$%
Vehicle Test	0.836	1.079	−22.5%
Simulation	0.92	1.02	−9.8%
Deviation ratio $\frac{(c_{q\_test}-c_{q\_sim})}{c_{q\_sim}}$%	−9%	6%	–

4.5. Results analysis on running mileage

Due to the strong wind and blown sand operating environment in the Urumqi running route, the sand particles are more easily swept up by the combined effect of the ambient strong wind and the wind that is disturbed by the train operation, and sand particles would be drawn into the air duct by the fan inside the ventilation equipment. Besides, part of the sand particles cannot pass through the grille filter. It will accumulate and block the filter during the long mileage operation, which greatly affects the equipment's ventilation. Therefore, the study of filter replacement intervals can prevent the equipment's ventilation from being affected by excessively clogging filters.

The average air volume of each day in several maintenance cycles is analysed, given in Figure 26. As the train operating mileage increased, the degree of filter clogging is increasingly serious, and the air volume decreased by 0.81% and 2.17% per kilometre in NTC and NHC conditions, respectively. Hence, the effect of running mileage on air volume in different running locations is shown in Equation (7).

$$\begin{cases} Q' = Q_0 - 0.0217S_c, & \text{Head End} \\ Q' = Q_0 - 0.0081S_c, & \text{Tail End} \end{cases} \tag{7}$$

where the air volume at the beginning of a maintenance cycle is denoted as $Q_0/(m^3/h)$, the current air volume is denoted as $Q'/(m^3/h)$, and the cumulative mileage of train is denoted as S_c/mileage.

Supposed the train runs to and fro on Urumqi-Lanzhou-Urumqi in one day after single maintenance based on the average static air volume in NHC condition, 4,580m^3/h, the filter clogging will make the converter's outlet air volume lower than the rated air volume when the operating mileage reached 22,818 km, and the filter needs to be replaced.

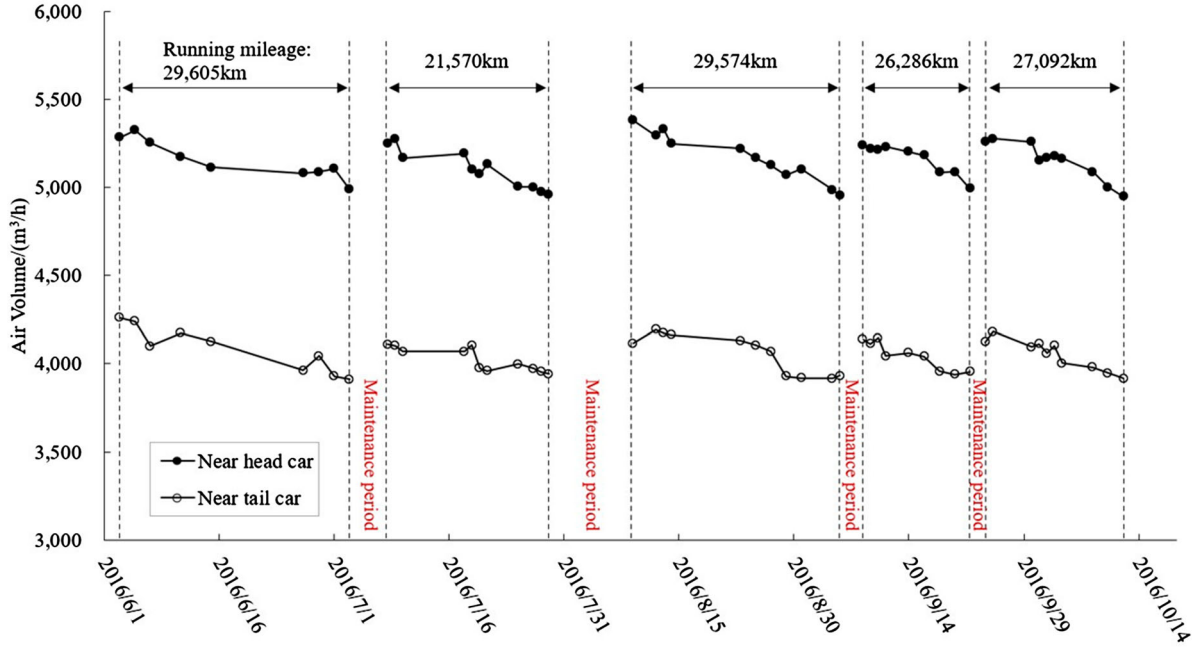

Figure 26. The effect of running mileage on air volume during several maintenance cycles.

5. Conclusions

In this paper, a two-step simulation method of ventilation characteristic around the equipment compartments underneath the Alpine HST using IDDES were performed. Besides, a real-vehicle tracking test using the TTPT was also conducted. The effects of EC, air vent location, and train mileage on ventilation performance are obtained. The conclusions are as follows:

In the numerical calculation,

(1) Ventilation performance can be influenced not only by the location of the EC, but also by the location of the facilities. The gradient of pressure variations between the external environment and the interior of the EC in the NHC condition is significant, which helps the airflow exchange. Moreover, the closer the bogie, the greater the pressure distribution is influenced by the location of the EC.
(2) The operation of the extractor fan is inhibited and the exhaust fan could work at a lower load, due to the pressure distribution and the shape of the AD. The airflow in the AD is pushed towards the external environment from the inlet and outlet vents. After the airflow meets the shape mutations, it rotates in two directions, which makes it hard to draw the air into the duct by the extractor fan.

In the real-vehicle test,

(1) The restraint effect occurs at the NTC condition compared to the train in static, the maximum restraint ratio is −16.4%, which is lower than the rated air volume.
(2) The air outlet volume of the converter near the head car is being promoted while it near the tail car is being inhibited, which is the same as the simulation result. The maximum deviation ratio between the test and simulation is 8%. Therefore, the measurement method in this study is relatively reliable.
(3) The filter clogging will make the converter's outlet air volume lower than the rated air volume when the operating mileage reached 22,818 km, and the filter needs to be replaced.

Therefore, in response to the foregoing study, the recommendations for the EC improvement and the research prospects are as follows:

(1) The key electrical facilities should be mounted in the middle of the EC. Its ventilation air duct should be smoother without shape mutations and the position of the inner fan should be placed based on the pressure distribution. Moreover, the filter replacement intervals need to be shortened by referring to the train operating mileages given in this article.
(2) Due to the relevant parameters are not available, the study of the temperature field in the area of the equipment compartment is not involved in this paper. Moreover, with the increase in train operating speed, it is important to investigate the influence of higher operating speed on the ventilation effect of

the equipment compartment. All of these need to be further investigated in the future.

Disclosure statement

No potential conflict of interest was reported by the author(s).

Funding

The authors gratefully acknowledge the financial support by the National Key R&D Program of China [Grant number 2022YFB4300601], and the Postgraduate Research Innovation Project of Hunan Province [Grant number 2022ZZTS0193]. This work was carried out in part using computing resources at the High-Performance Computing Centre of Central South University.

Data availability statement

The data that support the findings of this study are available from the corresponding author upon reasonable request.

CRediT authorship contribution statement

Yitong Wu: Methodology, Software, Validation, Formal Analysis, Data curation, Visualisation, Writing-Original Draft, Writing-Review & Editing. Wei Zhou: Conceptualisation, Methodology, Supervision. Xifeng Liang: Conceptualisation, Methodology. Dawei Chen: Funding acquisition. Xinchao Su: Methodology, Software, Formal Analysis, Writing-Review & Editing. Xiaobai Li: Formal Analysis. Fan Wu: Methodology. Sinisa Krajnović: Supervision.

References

Asadi, M., & Arezi, B. (2011). *Thermal design, modeling and simulation of air forced cooling heat sink for Thyristor Controlled Reactor (TCR)*. 2011 2nd Power Electronics. Drive Systems and Technologies Conference (pp. 625–631). https://doi.org/10.1109/PEDSTC.2011.5742495

Bai, G., & Gong, G. (2012). *The study of indoor air quality in train compartment*. 2012 Third International Conference on Digital Manufacturing & Automation (pp. 948–951). https://doi.org/10.1109/ICDMA.2012.224

Barone, G., Buonomano, A., Forzano, C., & Palombo, A. (2020). Enhancing trains envelope – heating, ventilation, and air conditioning systems: A new dynamic simulation approach for energy, economic, environmental impact and thermal comfort analyses. *Energy*, *204*, 117833. https://doi.org/10.1016/j.energy.2020.117833

Benjamin, S. F., & Roberts, C. A. (2002). Measuring flow velocity at elevated temperature with a hot wire anemometer calibrated in cold flow. *International Journal of Heat and Mass Transfer*, *45*(4), 703–706. https://doi.org/10.1016/S0017-9310(01)00194-6

Caré, I., Bonthoux, F., & Fontaine, J.-R. (2014). Measurement of air flow in duct by velocity measurements. *EPJ Web of Conferences*, *77*, 00010. https://doi.org/10.1051/epjconf/20147700010

Cheng, F., Xiong, X.-H., Tang, M.-Z., Li, X.-B., & Wang, X.-R. (2022). Impact of the gap distance between two adjacent external windshields of a high-speed train on surrounding flow characteristics: An IDDES study. *Engineering Applications of Computational Fluid Mechanics*, *16*(1), 724–745. https://doi.org/10.1080/19942060.2022.2046168

Cheng, N.-S., Hao, Z., & Tan, S. K. (2008). Comparison of quadratic and power law for nonlinear flow through porous media. *Experimental Thermal and Fluid Science*, *32*(8), 1538–1547. https://doi.org/10.1016/j.expthermflusci.2008.04.007

Comte-Bellot, G. (1976). Hot-wire anemometry. *Annual Review of Fluid Mechanics*, *8*(1), 209–231. https://doi.org/10.1146/annurev.fl.08.010176.001233

Dong, T., Minelli, G., Wang, J., Liang, X., & Krajnović, S. (2022). Numerical investigation of a high-speed train underbody flows: Studying flow structures through large-eddy simulation and assessment of steady and unsteady Reynolds-averaged Navier–Stokes and improved delayed detached eddy simulation performance. *Physics of Fluids*, 34(1), 015126. https://doi.org/10.1063/5.0075617

Feng, L., Wen, Y., Zhang, D., & Liu, D. (2022). Research on the optimization of shielding of the equipment compartment under the high-speed train. *2022 IEEE 2nd International Conference on Electronic Technology, Communication and Information (ICETCI)*, 224–227. https://doi.org/10.1109/ICETCI55101.2022.9832295

Ferranti, E., Chapman, L., Lowe, C., McCulloch, S., Jaroszweski, D., & Quinn, A. (2016). Heat-Related failures on southeast England's railway network: Insights and implications for heat risk management. *Weather, Climate, and Society*, *8*(2), 177–191. https://doi.org/10.1175/WCAS-D-15-0068.1

Foster, A., & Kinzel, M. (2021). Estimating COVID-19 exposure in a classroom setting: A comparison between mathematical and numerical models. *Physics of Fluids*, *33*(2), 021904. https://doi.org/10.1063/5.0040755

Georgiou, D. P., & Milidonis, K. F. (2014). Fabrication and calibration of a sub-miniature 5-hole probe with embedded pressure sensors for use in extremely confined and complex flow areas in turbomachinery research facilities. *Flow Measurement and Instrumentation*, *39*, 54–63. https://doi.org/10.1016/j.flowmeasinst.2014.07.005

Hu, J., Xuan, H. B., Kwok, K. C. S., Zhang, Y., & Yu, Y. (2018). Study of wind flow over a 6âĂŕm cube using improved delayed detached Eddy simulation. *Journal of Wind Engineering and Industrial Aerodynamics*, *179*, 463–474. https://doi.org/10.1016/j.jweia.2018.07.003

Jia, Q., Xia, C., Zang, J., Pan, D., Xu, J., & Gao, N. (2016). Numerical simulation on the temperature field in an equipment cabin of a high-speed railway train. *Building Simulation*, *9*(6), 689–700. https://doi.org/10.1007/s12273-016-0298-z

Jia, Q., Zang, J., Pan, D., Xia, C., Xu, J., & Gao, N. (2015). Analysis of high speed train equipment cabin temperature field based on numerical simulation. *Procedia Engineering*, *121*, 1954–1961. https://doi.org/10.1016/j.proeng.2015.09.187

Jiang, Y., Alexander, D., Jenkins, H., Arthur, R., & Chen, Q. (2003). Natural ventilation in buildings: Measurement in a wind tunnel and numerical simulation with large-eddy simulation. *Journal of Wind Engineering and Industrial Aerodynamics*, *91*(3), 331–353. https://doi.org/10.1016/S0167-6105(02)00380-X

Kaltenbach, H., Alonso, I., & Schober, M. (2008). A generic train-underfloor experiment for CFD validation. *BBAA VI International Colloquium on: Bluff Bodies Aerodynamics & Applications*, 20–24.

Kang, W., Trang, N. D., Lee, S. H., Choi, H. M., Shim, J. S., Jang, H. S., & Choi, Y. M. (2015). Experimental and numerical investigations of the factors affecting the S-type Pitot tube coefficients. *Flow Measurement and Instrumentation*, *44*, 11–18. https://doi.org/10.1016/j.flowmeasinst.2014.11.006

Kotelnikov, A. L., Bazhenova, T. V., Bivol, G. Y., & Lenkevich, D. A. (2017). Impact on blockage of an airflow containing solid particles. *High Temperature*, *55*(1), 162–164. https://doi.org/10.1134/S0018151X17010138

Li, H. (2020). The study of thermal environment during the movement of Air-conditioned train. *IOP Conference Series: Materials Science and Engineering*, *735*(1), 0012080. https://doi.org/10.1088/1757-899X/735/1/012080

Li, X., Wu, F., Tao, Y., Yang, M., Newman, R., & Vainchtein, D. (2019). Numerical study of the air flow through an air-conditioning unit on high-speed trains. *Journal of Wind Engineering and Industrial Aerodynamics*, *187*, 26–35. https://doi.org/10.1016/j.jweia.2019.01.015

Li, Y. N., & Wang, Y. (2015). Study on control model of Air-conditioning system of Air-conditioned train in qinghai-Tibet railway. *Applied Mechanics and Materials*, *713–715*, 905–908. https://doi.org/10.4028/www.scientific.net/AMM.713-715.905

Liang, X.-F., Chen, G., Li, X.-B., & Zhou, D. (2020). Numerical simulation of pressure transients caused by high-speed train passage through a railway station. *Building and Environment*, *184*, 107228. https://doi.org/10.1016/j.buildenv.2020.107228

Liu, H., Zhang, S., Liang, X., & Zou, Y. (2022). The effect of covering structure in pantograph sinking platform on the aerodynamics of high- speed train. *Engineering Applications of Computational Fluid Mechanics*, *16*(1), 2157–2175. https://doi.org/10.1080/19942060.2022.2133517

Liu, W., Deng, Q., Huang, W., & Liu, R. (2011). Variation in cooling load of a moving air-conditioned train compartment under the effects of ambient conditions and body thermal storage. *Applied Thermal Engineering*, *31*(6-7), 1150–1162. https://doi.org/10.1016/j.applthermaleng.2010.12.010

López González, L., Galdo Vega, M., Fernández Oro, J. M., & Blanco Marigorta, E. (2014). Numerical modeling of the piston effect in longitudinal ventilation systems for subway tunnels. *Tunnelling and Underground Space Technology*, *40*, 22–37. https://doi.org/10.1016/j.tust.2013.09.008

Maier, J., Marggraf-Micheel, C., Dehne, T., & Bosbach, J. (2017). Thermal comfort of different displacement ventilation systems in an aircraft passenger cabin. *Building and Environment*, *111*, 256–264. https://doi.org/10.1016/j.buildenv.2016.11.017

Pan, A.-X., Gong, Y., & Yang, Z.-G. (2021). Failure analysis on abnormal leakage of radiator for high-speed train transformer. *Engineering Failure Analysis*, *129*, 105673. https://doi.org/10.1016/j.engfailanal.2021.105673

Paradot, N., Talotte, C., Garem, H., Delville, J., & Bonnet, J.-P. (2009). *A comparison of the numerical simulation and experimental investigation of the flow around a high speed train*. ASME 2002 Joint U.S.-European Fluids Engineering Division Conference (pp. 1055–1060). https://doi.org/10.1115/FEDSM2002-31430

Schmeling, D., & Bosbach, J. (2017). On the influence of sensible heat release on displacement ventilation in a train compartment. *Building and Environment*, *125*, 248–260. https://doi.org/10.1016/j.buildenv.2017.08.039

Shen, J., Qin, X., & Wang, Y. (2018). High-speed permanent magnet electrical machines — applications, key issues and challenges. *CES Transactions on Electrical Machines and Systems*, *2*(1), 23–33. https://doi.org/10.23919/TEMS.2018.8326449

Shur, M. L., Spalart, P. R., Strelets, M. K., & Travin, A. K. (2008). A hybrid RANS-LES approach with delayed-DES and wall-modelled LES capabilities. *International Journal of Heat and Fluid Flow*, *29*(6), 1638–1649. https://doi.org/10.1016/j.ijheatfluidflow.2008.07.001

Soper, D., Flynn, D., Baker, C., Jackson, A., & Hemida, H. (2018). A comparative study of methods to simulate aerodynamic flow beneath a high-speed train. *Proceedings of the Institution of Mechanical Engineers, Part F: Journal of Rail and Rapid Transit*, *232*(5), 1464–1482. https://doi.org/10.1177/0954409717734090

Suzuki, M., Ido, A., Sakuma, Y., & Kajiyama, H. (2008). Full-Scale measurement and numerical simulation of flow around high-speed train in tunnel. *Journal of Mechanical Systems for Transportation and Logistics*, *1*(3), 281–292. https://doi.org/10.1299/jmtl.1.281

Tanghong, L., & Gang, X. (2010). *Test and improvement of ventilation cooling system for high-speed train*. 2010 International Conference on Optoelectronics and Image Processing (Vol. 2, pp. 493–497). https://doi.org/10.1109/ICOIP.2010.55.

Valger, S. (2022). Estimation of pollutant dispersion around a building within non-isothermal boundary-layer using detached eddy simulation. *Thermal Science*, *26*(2 Part C), 2013–2025. https://doi.org/10.2298/TSCI211123046V

Wang, H., Lin, M., & Chen, Y. (2014). Performance evaluation of air distribution systems in three different China railway high-speed train cabins using numerical simulation. *Building Simulation*, *7*(6), 629–638. https://doi.org/10.1007/s12273-014-0168-5

Wang, J., Minelli, G., Dong, T., Chen, G., & Krajnović, S. (2019). The effect of bogie fairings on the slipstream and wake flow of a high-speed train. An IDDES study. *Journal of Wind Engineering and Industrial Aerodynamics*, *191*, 183–202. https://doi.org/10.1016/j.jweia.2019.06.010

Wang, J., Minelli, G., Miao, X., Zhang, J., Wang, T., Gao, G., & Krajnović, S. (2021). The effect of bogie positions on the aerodynamic behavior of a high-speed train: An IDDES study. *Flow, Turbulence and Combustion*, *107*(2), 257–282. https://doi.org/10.1007/s10494-020-00236-9

Wang, J., Zhang, J., Zhang, Y., Xie, F., Krajnović, S., & Gao, G. (2018). Impact of bogie cavity shapes and operational environment on snow accumulating on the bogies of high-speed trains. *Journal of Wind Engineering and Industrial Aerodynamics*, *176*, 211–224. https://doi.org/10.1016/j.jweia.2018.03.027

Wang, S., Burton, D., Herbst, A., Sheridan, J., & Thompson, M. C. (2018). The effect of bogies on high-speed train slipstream and wake. *Journal of Fluids and Structures*, *83*, 471–489. https://doi.org/10.1016/j.jfluidstructs.2018.03.013

Wang, X., Yang, Q., He, Y., & Zhang, S. (2022). Numerical investigation on aerodynamic and electromagnetic influence of shape of The grilles in a rectangular duct.

Journal of Physics: Conference Series, *2235*(1), 0012037. https://doi.org/10.1088/1742-6596/2235/1/012037

Xu, L., Pan, Y., & Liu, T. (2014). Study of the T type back-supported tube and its application in EMU flow test. *Journal of Experiments in Fluid Mechanics*, *28*(5), 99–103. https://doi.org/10.11729/syltlx20140010 [In Chinese].

Yang, A. M., Li, Y. F., Xing, H. W., Zhang, L., Feng, L. J., Li, Y. H., & Cheng, F. Y. (2017). Numerical study on aerodynamic characteristics of high-speed trains with considering thermal-flow coupling effects. *Journal of Vibroengineering*, *19*(7), 5606–5626. https://doi.org/10.21595/jve.2017.18778

Yang, S., Xiang, D., Bryant, A., Mawby, P., Ran, L., & Tavner, P. (2010). Condition monitoring for device reliability in power electronic converters: A review. *IEEE Transactions on Power Electronics*, *25*(11), 2734–2752. https://doi.org/10.1109/TPEL.2010.2049377

Yao, Z., Xiao, J., & Jiang, F. (2012). Characteristics of daily extreme-wind gusts along the Lanxin Railway in Xinjiang, China. *Aeolian Research*, *6*, 31–40. https://doi.org/10.1016/j.aeolia.2012.07.002

Zhang, J., Adamu, A., Han, S., Wang, F., Gao, G., & Gidado, F. (2023). A numerical investigation of inter-carriage gap configurations on the aerodynamic performance of a wind-tunnel train model. *Proceedings of the Institution of Mechanical Engineers, Part F: Journal of Rail and Rapid Transit*, *237*(6), 734–750. https://doi.org/10.1177/09544097221136914

Zhang, J., Adamu, A., Su, X., Guo, Z., & Gao, G. (2022). Effect of simplifying bogie regions on aerodynamic performance of high-speed train. *Journal of Central South University*, *29*(5), 1717–1734. https://doi.org/10.1007/s11771-022-4948-2

Zhang, J., Gidado, F., Adamu, A., Guo, Z., & Gao, G. (2023). An investigation on the wake flow of a generic ship using IDDES: The effect of computational parameters. *Ocean Engineering*, *271*, 113644. https://doi.org/10.1016/j.oceaneng.2023.113644

Zhang, J., Guo, Z., Han, S., Krajnović, S., Sheridan, J., & Gao, G. (2022). An IDDES study of the near-wake flow topology of a simplified heavy vehicle. *Transportation Safety and Environment*, *4*(2), tdac015. https://doi.org/10.1093/tse/tdac015

Zhang, J., Li, J., Tian, H., Gao, G., & Sheridan, J. (2016). Impact of ground and wheel boundary conditions on numerical simulation of the high-speed train aerodynamic performance. *Journal of Fluids and Structures*, *61*, 249–261. https://doi.org/10.1016/j.jfluidstructs.2015.10.006

Zhang, J., Wang, F., Han, S., Huang, T., Gao, G., & Wang, J. (2022). An investigation on the switching of asymmetric wake flow and the bi-stable flow states of a simplified heavy vehicle. *Engineering Applications of Computational Fluid Mechanics*, *16*(1), 2035–2055. https://doi.org/10.1080/19942060.2022.2130432

Zhang, N., Lu, Z., Niu, J., & Zhou, D. (2017). Temperature field in equipment cabin of high-speed train in the harsh wind environment and extreme temperature condition. *DEStech Transactions on Engineering and Technology Research*, icia. https://doi.org/10.12783/dtetr/icia2017/15714

Zhang, S. (2007). *Crh2 electric multiple unit*. *China Railway Publishing House Co., Ltd*. ISBN 978-7-113-08189-8 (in Chinese).

Zhou, W., Chen, L., Wang, Z., Ding, S., & Shan, Y. (2019). Aerodynamic load spectrum and fatigue behaviour of high-speed train's equipment cabin. *Fatigue & Fracture of Engineering Materials & Structures*, *42*(11), 2579–2595. https://doi.org/10.1111/ffe.13126

Zhu, J. Y., & Hu, Z. W. (2017). Flow between the train underbody and trackbed around the bogie area and its impact on ballast flight. *Journal of Wind Engineering and Industrial Aerodynamics*, *166*, 20–28. https://doi.org/10.1016/j.jweia.2017.03.009